UNIVERSITÀ DEGLI STUDI DI PADOVA

SCUOLA DI SCIENZE
Dipartimento di Geoscienze
Direttore Prof. Nicola Surian

TESI DI LAUREA MAGISTRALE IN
Geologia Ambientale E Dinamica Della Terra (LM-74)
Curriculum Earth Dynamics

Middle-Late Jurassic ooids in calciturbidites of the Belluno Basin at the switch from Aragonite Sea II to Calcite Sea II, and its relation with the Jurassic carbon cycle

Relatore: Prof. Nereo Preto
Correlatore: Dr. Ingrid Urban

Laureanda: Omneya Ahmed
Matricola: 2085785

ANNO ACCADEMICO 2024-2025

Dedicato a Te, o Madre mia, e al Tuo Bambino… ♡

Contents

Abstract

The Middle-to-Late Jurassic marks a crucial interval in Earth's history, characterized by significant shifts in seawater chemistry, sedimentary environments, and the global carbon cycle. This study investigates the occurrence, size distribution, and mineralogical properties of ooids preserved in calciturbidites from the Belluno Basin, a key region in the western Tethys. The research focuses on the post-transition from the Aragonite Sea II to the Calcite Sea II to assess its implications for carbonate sedimentation and Jurassic carbon cycling.

Fieldwork conducted in the Belluno Basin enabled the collection of representative samples, which were analyzed using petrographic microscopy, isotopic geochemistry, and scanning electron microscopy for nannofossil biostratigraphy. The results reveal considerable variations in ooid size distribution throughout the Oxfordian and Kimmeridgian, with a general increase in size during the latter. Mineralogical analysis confirms a predominance of calcitic ooids, reinforcing the transition to a calcite-dominated marine environment—without any detectable traces of aragonite ooids. Isotopic data further align with regional and global Jurassic trends, indicating that ooid formation and preservation were shaped by broader paleoceanographic and climatic influences.

By illuminating the variables that governed ooid formation, the timing of significant geochemical alterations, and their function in the Jurassic carbon cycle, this study advances our knowledge of Jurassic carbonate sedimentology. These discoveries provide important insights into how carbonate platforms changed and how the Tethyan realm's paleoenvironment changed during this dynamic period.

Riassunto

Il Giurassico medio-superiore rappresenta un intervallo cruciale nella storia della Terra, caratterizzato da significativi cambiamenti nella chimica delle acque marine, negli ambienti sedimentari e nel ciclo globale del carbonio. Questo studio analizza la presenza, la dimensione e la mineralogia degli ooidi conservati nelle calciturbiditi del Bacino Bellunese, una regione chiave nel dominio occidentale della Tetide. La ricerca si concentra sul periodo successivo alla transizione dal Mare Aragonite II al Mare Calcite II, valutandone le implicazioni sulla sedimentazione carbonatica e sul ciclo del carbonio durante il Giurassico.

Le campagne condotte nel Bacino Bellunese hanno permesso di raccogliere campioni rappresentativi, successivamente analizzati mediante microscopia petrografica, geochimica isotopica e microscopia elettronica a scansione per la biostratigrafia dei nannofossili. I risultati rivelano variazioni significative nella distribuzione dimensionale degli ooidi tra l'Oxfordiano e il Kimmeridgiano, con una tendenza generale all'aumento delle dimensioni in quest'ultimo. L'analisi mineralogica conferma la predominanza di ooidi calcitici, consolidando l'evidenza di un mare calcite nel giurassico superiore, senza alcuna traccia rilevabile di ooidi aragonitici. Inoltre, i dati isotopici risultano coerenti con le tendenze giurassiche regionali e globali, suggerendo che la formazione e la conservazione degli ooidi siano state influenzate da più ampi fattori paleoceanografici e climatici.

Illuminando le variabili che hanno regolato la formazione degli ooidi, la tempistica delle principali alterazioni geochimiche e il loro ruolo nel ciclo del carbonio giurassico, questo studio contribuisce ad approfondire la conoscenza della sedimentologia carbonatica del Giurassico. Queste scoperte forniscono importanti informazioni sull'evoluzione delle piattaforme carbonatiche e sulle trasformazioni paleoambientali nel dominio tetideo durante questo dinamico periodo.

1. Introduction

1.1 Motivation

Ooids are tiny, spherical to ellipsoidal carbonate grains usually made up of concentric calcium carbonate laminae encircling a nucleus (Fig. 1), which is frequently a grain of sand, a piece of shell, or another tiny particle. The precipitation of calcium carbonate (either aragonite or calcite) from seawater, most likely due to agitation in shallow marine habitats, forms these laminae, which differ in thickness and content (Bathurst 1975; Flügel 2010). Depending on the growing conditions, the laminae may exhibit a variety of microstructures, such as radial-fibrous, tangential, or micritic textures. Ooids can be clearly identified under a microscope thanks to their interior structure, which also helps to differentiate them from other carbonate grains.

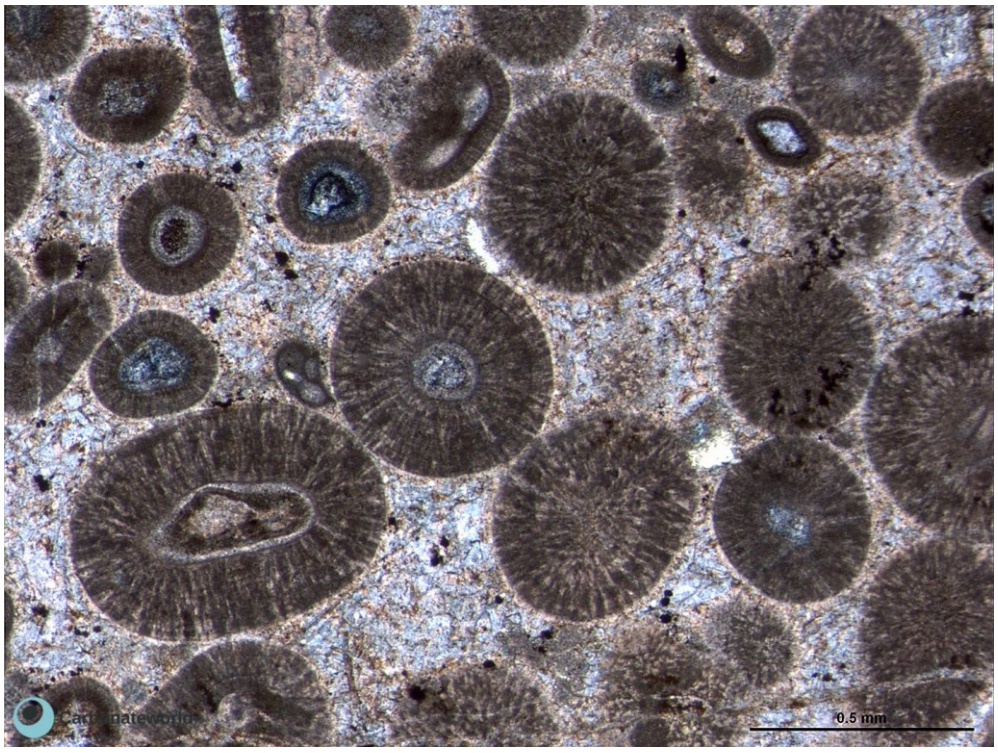

Figure 1. CarbonateWorld. (n.d.). Radial ooids in a grainstone from the Pennsylvanian of Asturias, Northern Spain. Retrieved February 11, 2025, from https://carbonateworld.com

Geologists have been captivated by these fascinating sedimentary formations for many years because of their distinct formation processes and capacity to act as proxies for

historical environmental conditions (Flügel 2010). The interaction of physical, chemical, and biological elements—such as water agitation, calcium carbonate saturation, and microbial activity—controls their formation (Bathurst 1975). Ooids are particularly significant in geological records from the Precambrian to the Mesozoic era, with a marked decline in their abundance after the Jurassic (Tucker & Wright 1990; Vulpius & Kiessling 2006). This post-Mesozoic scarcity prompts questions about the connection between ooid generation, seawater chemistry, and environmental changes.

It has been proposed that the saturation condition of seawater with respect to calcium carbonate minerals is correlated with the size of ooids in particular. While smaller ooids may imply less favorable conditions for carbonate precipitation, larger ones may indicate higher levels of supersaturation (James et al., 1999). Moreover, environmental changes including sea-level variations, basin connections, and nutrient levels might be reflected in their size and frequency. According to middle-to-late Jurassic records, ooids were more numerous in the western Tethys Ocean than in other areas, suggesting that the chemistry and dynamics of seawater varied by region (Kiessling 2009). This raises interesting questions about the spatial heterogeneity of ooid formation during this crucial time. In this case, the Belluno Basin provides an unrivaled opportunity to study the occurrence and size variations of middle to Late Jurassic ooids recorded in calciturbidites. This thesis investigates their abundance and size to understand how these parameters align with existing literature. Additionally, it explores whether changes in ooid type and size coincide with isotopic variations, which advances our knowledge of Jurassic carbon cycling.

The mineralogical composition of ooids is known to have evolved through geological time, reflecting changes in seawater chemistry. Ooids usually formed as aragonitic grains during periods of "Aragonite Sea," defined by greater Mg/Ca ratios dissolved in seawater. In contrast, calcitic ooids were more prevalent during "Calcite Sea" intervals, with a lower Mg/Ca ratio (Sandberg 1983; Vulpius & Kiessling 2006). The Middle-to-Late Jurassic, a transitional phase between Aragonite Sea II and Calcite Sea II (Fig. 2), presents a unique opportunity to investigate whether ooids from this interval have the expected calcitic composition or preserve traits of earlier aragonitic mineralogy. Understanding this mineralogical transition is crucial to understanding the relationship between seawater chemistry and carbonate mineralogy, as well as the mechanisms governing sedimentary

environments throughout this time. This study examines the petrographic characteristics of ooids from the Belluno Basin to see whether they show anomalies that contradict our current understanding or fit into the widely recognized models of mineralogical transitions.

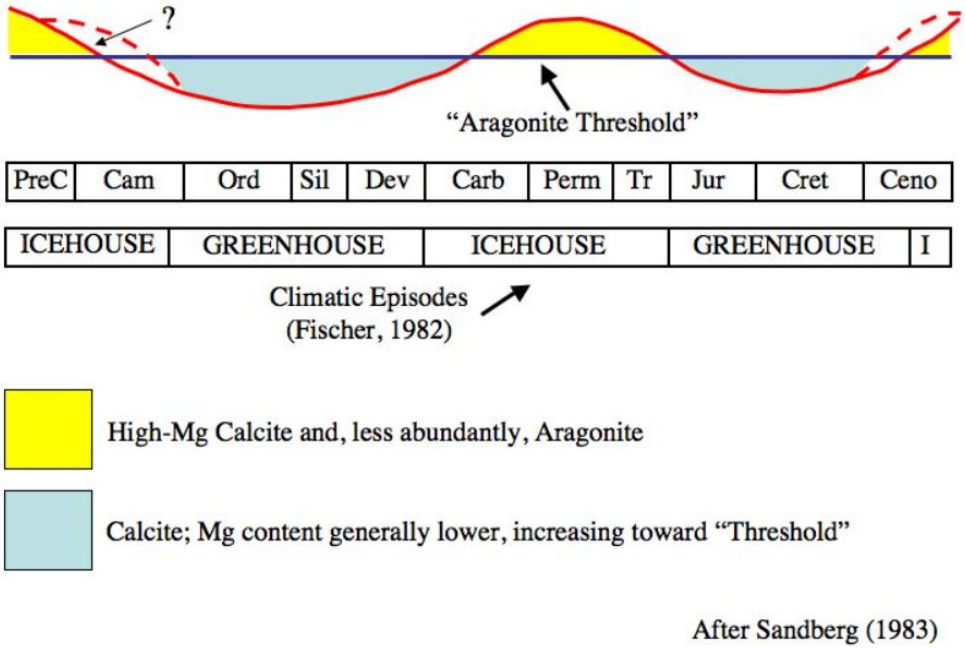

Figure 2: Aragonite threshold and climatic episodes over geologic time. Adapted from Sandberg (1983), after Fischer (1982). Image created by Mark A. Wilson (Department of Geology, The College of Wooster), retrieved from Wikipedia.

The Belluno Basin in the western Tethys realm provides an excellent natural laboratory for examining these issues. It is a well-documented region where carbonate grains found in calciturbidites were generated in shallow marine settings and then transported to deeper environments via sedimentary processes. This geological setting preserves a rich archive of carbonate grains, especially ooids, which can reveal information about the regional and global variables that influenced their formation. This study integrates size distribution measurements, petrographic analysis, and isotopic data to shed light on the dynamics of ooid generation and how they relate to the chemistry of seawater and the carbon cycling of the Jurassic Period.

In this thesis, we seek to accomplish two key goals: (1) to investigate the ooids' diameters and abundance in the Belluno Basin and assess their correlation with local and global

Jurassic data, and (2) to investigate the ooids' mineralogical properties to determine whether they are consistent with the Middle-to-Late Jurassic calcite-dominant model. In addition to improving our knowledge of the Jurassic carbon cycle, this dual approach offers critical insights into the interactions among carbonate mineralogy, sedimentary processes, and seawater chemistry. This study helps place western Tethys carbonate production within the larger framework of Jurassic carbonate sedimentology.

1.2. Geological setting

1. 2. 1. Paleogeography and Definition of the Belluno Basin

The Belluno Basin, a 20–50 km wide narrow basin in northern Italy's Southern Alps (Picotti & Cobianchi 2017), is a key paleogeographic feature that was formed during the Late Triassic and Early Jurassic (Bernoulli & Jenkyns 1974; Winterer & Bosellini 1981) by the breakup of the Pangea supercontinent and the subsequent rifting of the Adria passive margin (Bertotti et al., 1993; Castellarin et al., 1992).

It developed as a deep-marine basin that led into the Venetian Alps as a "tongue of the ocean" formed by carbonate platforms, Trento to the west and Friuli to the east (Fig. 3; Bosellini et al., 1981), However, this was only true until the Trento Platform drowned and became a submerged plateau during the Bajocian (Middle Jurassic), leaving the Friuli to the east as the only productive carbonate platform (Picotti & Cobianchi 2017).

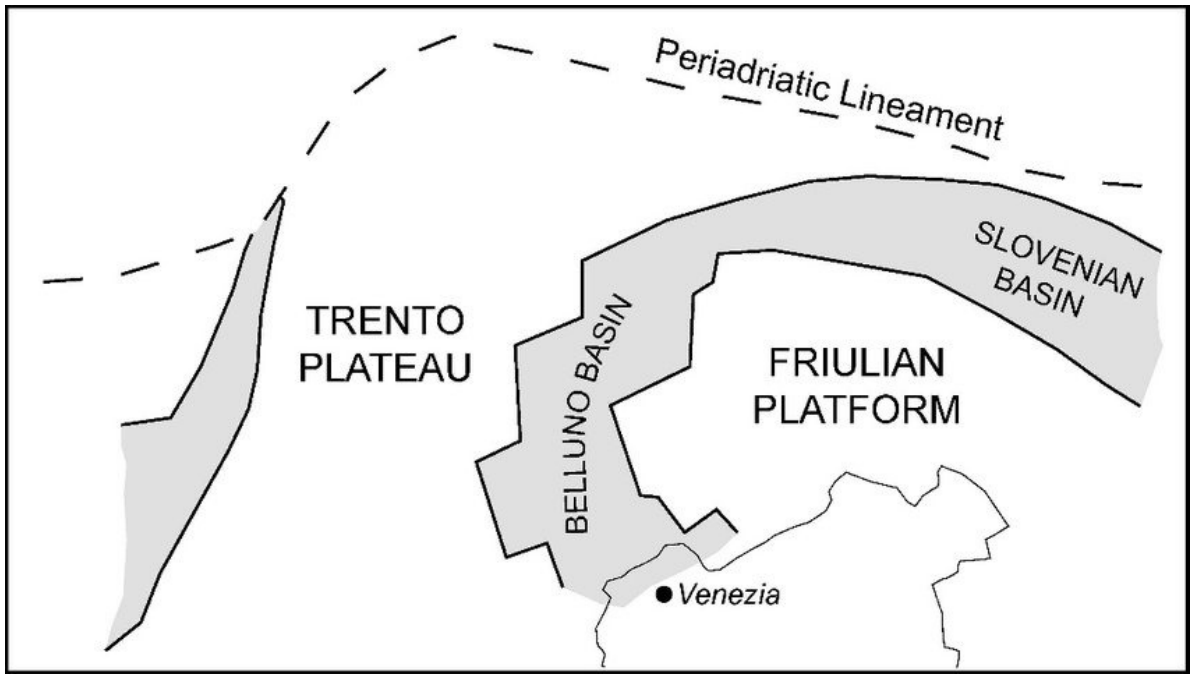

Figure 3. Paleogeographic map of the eastern Alps during the Jurassic (modified from Masetti et al. 1998), (Stefani et al., 2007).

This paleogeographic structure made it easier for sediments to accumulate, which documents important changes in ocean chemistry, such as the Middle to Late Jurassic transition from the Aragonite Sea II to the Calcite Sea II (Picotti & Cobianchi, 2017).

1. 2. 2. Lithological Succession in the Belluno Basin

The Middle to Late Jurassic lithological succession within the Belluno Basin starts with 1) The Igne Fm, which formed above the Soverzene Fm of the Lower Jurassic. It comprises limestone and marl couplets with thin bedding that formed possibly during basin starvation. With sponge spicules, pelagic bivalves, ostracods, echinoid plates, lagenid foraminifers, and ammonoid protoconchs, the limestones are peloidal wacke-packstone that pass upwards to dolomitic limestones - dolostones (Picotti & Cobianchi 2017). According to Cobianchi (2002), the Igne Fm. is attributed to the Early Toarcian to Bajocian, based on calcareous nannofossils biostratigraphy.

Then the condition at that point started to change, ooids dominated the platform carbonate production, at least since the latest Bajocian–earliest Bathonian. Rapid infilling of the previous rift basin was made possible by a regressional trend up to the Middle Bathonian. Up to the Lower Oxfordian, non-skeletal grains continued to dominate the platform's sequential aggradation. The Middle Oxfordian to Lower Kimmeridgian was a time of recovery of the palaeoceanographic conditions allowing the construction of a hydrozoan/coral-rich platform (Picotti & Cobianchi, 2017) and that will explain the lithology of the next two formations.

2) Vajont Oolitic Limestone represents one of the peculiar features of the Belluno Basin. It abruptly overlains the Igne Fm., its thickness spans from a few meters to 400 m and it consists of poorly bedded to massive oolitic lime grainstones and lime packstones with frequent oncoids, peloids, lumps, micritic intraclasts, and skeletal grains (Fig. 4; Picotti & Cobianchi 2017), deposited through gravity-flow processes that carried oolitic sands into slope and basin environments from the Friuli platform's western border (Bosellini & Masetti 1972; Bosellini et al., 1981). Its age is Bathonian (Mattioli & Erba 1999; Cobianchi 2002).

3) Fonzaso Fm. overlies the Vajont Limestone and grades upward into the Maiolica Fm., and is distinguished by cherty limestones and marls, rich in grey and red chert, interbedded with carbonate turbidites. From a lower part of the unit, which is primarily composed of ooids, to a middle section that is enriched in skeleton pieces, the composition of the resedimented carbonate grains changes (Fig. 4). Picotti & Cobianchi (2017) subdivided the Fonzaso Fm. into informal members using this change.

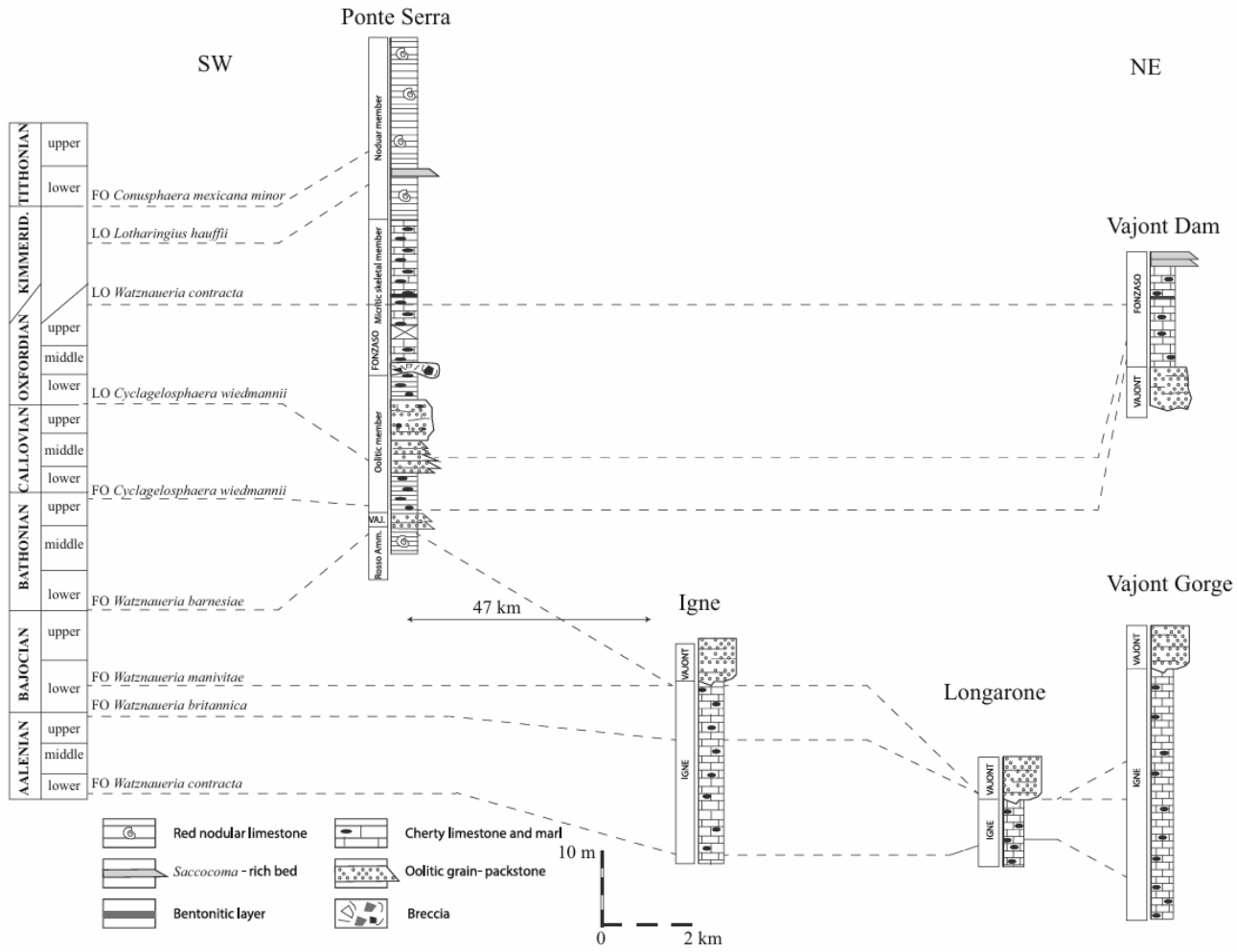

Figure 4. Studied stratigraphic sections along one of the profiles in the Belluno Basin (Picotti & Cobianchi, 2017).

I) "The lower oolitic member" consists of thin-bedded red and green cherty limestones, with red marly interbeds and red chert. These layers are interbedded locally with white peloidal and oolitic grainstone showing parallel and wavy lamination. Grains are mostly composed of radial ooids, with a small amount of agglutinated foraminifers and miliolids. The age of this member spans from the Upper Bathonian to the Lower Oxfordian,

according to the distribution of nannoplankton in the sections under study by Cobianchi (2002) and Picotti & Cobianchi (2017).

II) “The micritic skeletal member” begins with a bioclastic matrix supported breccia, varies in thickness from 1 to 10 m, grading to a grainstone at the top. Corals, calcareous sponges, calcareous algae, and micritic intraclasts are all found in clasts, which are embedded in a white micritic matrix. A thinning upward interval of well-bedded light grey mudstones and bioclastic grainstones covers this base breccia. Grey-green lime mudstones rich in radiolarians, with marly interbeds and an abundance of chert nodules and ribbons, follow. And according to the distribution of nannoplankton in the sections under study by Cobianchi (2002) and Picotti & Cobianchi (2017), this member covers the Middle Oxfordian to the Kimmeridgian.

III) “The nodular member” The skeletal member grades upward into an interval of thin bedded to nodular reddish radiolarian-rich limestones with green and red marly interbeds (Picotti & Cobianchi 2017).

As is frequently the case in the Kimmeridgian to Tithonian, saccocoma-rich beds do occur (Nicosia & Parisi 1979). Some thin beds of whitish bentonites are interbedded, derived from original volcanic ashes found in the upper part of this member (Bernoulli & Peters 1970). It has been identified as well as a Kimmeridgian to Early Tithonian member by Della and Martire (1985).

The Fonzaso Fm. Is overlain by the Lower Cretaceous Maiolica Fm (Masetti et al., 2012; Picotti & Cobianchi 2017). The detailed study of the nannofossil content attributed the whole formation to the Late Bathonian–Early Tithonian interval (Cobianchi & Picotti 2002).

1. 2. 3. The Outcrop of the study area

The site of the fieldwork was at a relatively well-exposed outcrop near the small town of Tovena, located at the depocenter of the Belluno Basin at coordinates 45°58'58"N 12°10'49"E, close to Vittorio Veneto (Fig. 5). This site was selected as one of the most

accessible and stratigraphically complete sections within the basin, capturing key facies transitions relevant to the study's objectives. The tilted outcrop lies along a forest-white road, starting from an open space and being exposed on the roadside excavated wall. This positioning provided fairly continuous exposure to the stratigraphic layers, enabling detailed observation and systematic sampling.

Figure 5. Satellite imagery of the outcrop and Trovena Hamlet, Italy, showing the outcrop (marked in red). Source: Google Earth (2025).

This study contributes to the geological mapping works for the geological map 084 - Vittorio Veneto, at a scale of 1:50,000. The goal of the mapping project is to enhance our understanding of the region's stratigraphy and tectonic history, with the Belluno Basin which is serving as a key area for investigating Jurassic carbonate systems and their paleoceanographic significance.

2. Materials and methods

2.1. Fieldwork and facies analysis

Field investigations took place near the village of Tovena in Belluno Basin to collect representative samples of Middle to Late Jurassic ooids within calciturbidites. To document lithological variances and sedimentary facies, a stratigraphic section was measured and described in detail. Changes in texture, composition, and sedimentary structures were used to identify key stratigraphic units. The presence of calciturbidites containing ooids served as a guide for sampling, and lateral and vertical facies differences received special attention.

To ensure coverage of important facies transitions and for stable isotopic analyses, a total of 100 samples were gathered from different stratigraphic intervals. To maintain the integrity of the samples, they were carefully labeled before being brought to the lab. To make thin-section preparation easier, rock samples were cut into smaller blocks by a lapidary slab saw (Fig. 6) and polished by a Forcipol Grinding and Polishing Machine. Petrolab srl (an external lab) prepared the thin sections. To get the best optical clarity, samples were polished, ground to the proper thickness (~30 μm), and coated with resin. A total of thirty-one thin sections were prepared for microscopic examination. and then were photographed using a slide scanner.

Thin sections were analyzed under a petrographic microscope to study the composition and the facies of the rocks in general and the texture and internal structures of the ooids in particular. Special focus was placed on distinguishing micritic vs. radial ooids, identifying concentric laminae, and observing any diagenetic alterations.

Finally, a geological stratigraphic log for the whole outcrop was sketched by Inkscape to demonstrate the lithology, biostratigraphy, sedimentary features, and stable isotopic composition of the outcrop.

Figure 6. Part of the cutting process for thin-section preparation.

2.2. Isotopic analyses

A total of (72) samples were selected for carbonate stable carbon and oxygen isotope analyses. Samples were prepared and pre-treated to remove potential contaminants and ensure accurate isotopic measurements.

For stable isotope analyses, 94 powdered samples from different components [74 samples for bulk, 9 for veins, 5 for sponges, and 4 for grains] were microdrilled with a hand-held dentist drill, targeting separately late calcite veins, late cement filling primary cavities and shell replacing calcite cement, and bulk rock unaffected by fracturing. About 5-10 mg of powder was obtained per sample.

Figure 7. Thermo Delta V Advantage isotope ratio mass spectrometer (IRMS) at the Department of Geosciences, University of Padova, which was used during the analysis.

A Thermo Delta V Advantage Isotope Ratio Mass Spectrometer (IRMS) located in the University of Padova's Department of Geoscience was utilized to conduct analyses for the stable isotopes of carbon and oxygen (Fig. 7). Samples were weighted in borosilicate

glass vials with rubber sept. 0.180–0.350 mg of powder were prepared (Fig. 8), and 20 drops of >99% orthophosphoric acid were then injected to develop CO2, which interacted with the carbonate for around three hours at 70 ºC in a Gasbench II device. An internal standard (white Carrara marble Maq 1: $\delta^{13}C$ = -2.58‰; $\delta^{18}O$ = -1.15‰ VPDB) that is periodically calibrated against NBS 19 was then used to calibrate the measured raw $\delta^{13}C$ and $\delta^{18}O$. In accordance with Kim et al. (2015), a two-point normalization was carried out for samples whose isotopic values were significantly different from those of NBS 19 (such as vein calcite). These samples were run alongside a second internal standard (commercial synthetic carbonate Supp: $\delta^{13}C$ = -49.69‰; $\delta^{18}O$ = -16.38‰ VPDB).

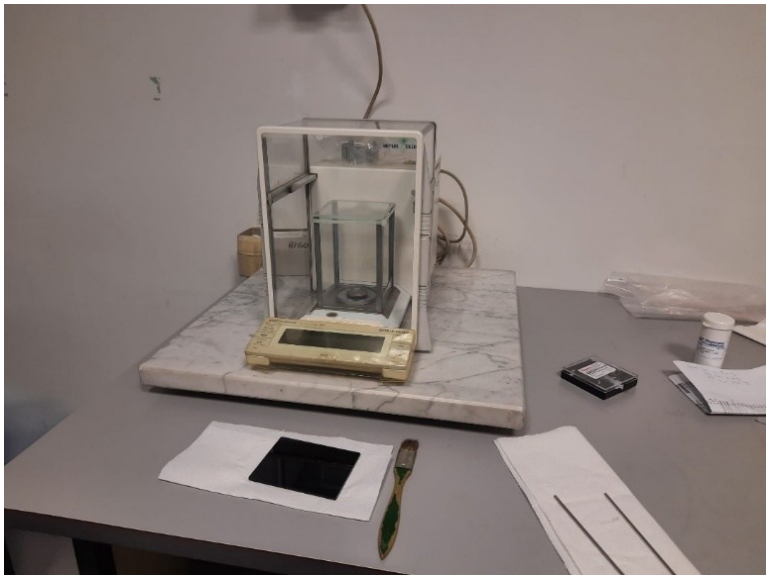

Figure 8. A precision scale was used to weigh rock powder samples before analysis with the IRMS.

Periodically, the international standards NBS 18, NBS 19, and L-SVEC are used to calibrate the internal standard Supp. Coplen et al. (2006) provide the nominal values of the international standards that were used for these calibrations. A third internal standard was performed for quality assurance during the analysis period, and it was repeated with precisions of better than 0.07‰ for $\delta^{13}C$ and better than 0.08‰ for $\delta^{18}O$.

2.3. SEM for nannofossils

At the beginning, a total of 23 samples were collected along the entire geological log, to ensure a representative coverage of the stratigraphic section. The initial rock samples were trimmed into small cubes (~1 cm^3) using a precision trim saw to ensure manageable sizes for further processing. Each cube was polished on one surface to create a flat, smooth base for mounting. The polished samples were adhered to glass slides using epoxy resin to stabilize them during subsequent treatments (Fig. 9).

Mounted samples underwent a quick immersion in a dilution of strong acid (with a concentration of 0.3) to etch the surface lightly for 10 to 20 seconds, to enhance the visibility of microstructures. Following acid treatment, samples were ultrasonically washed in deionized water to remove residual particles, dust, and contaminants that may be formed from the reaction (Fig. 10).

After the initial preparation, samples were examined under a scanning electron microscope to identify those with well-preserved nannofossil assemblages. From the initial 23 samples, a subset of (12) samples were chosen as suitable ones for more detailed analysis.

The twelve selected samples were fractured manually to create thin, fresh samples with uneven surfaces, exposing fresh surfaces ideal for SEM imaging. The fragments were then mounted on aluminum stubs using conductive carbon tape. Samples were coated with a thin layer of (~10–20 nm) gold using a sputter coater to enhance conductivity and improve imaging quality during SEM analysis (Fig. 11). The SEM analyses were conducted at two places at the Geoscience Department and “CEASC” Centro di Analisi e Servizi Per la Certificazione (University of Padova), using a Zeiss EVO LS 10 Scanning Electron Microscope equipped with secondary electron and backscattered electron detectors for high-resolution imaging (Fig. 12).

After checking them, 4 samples out of the 12 samples were neglected because they didn’t show prominent results, and another 2 samples were chosen from the etched specimen. The determinations of nannofossil taxa and assemblages were carried out by Prof. Miriam

Cobianchi (University of Pavia) as part of the collaborative studies contributing to the geological map 084 - Vittorio Veneto.

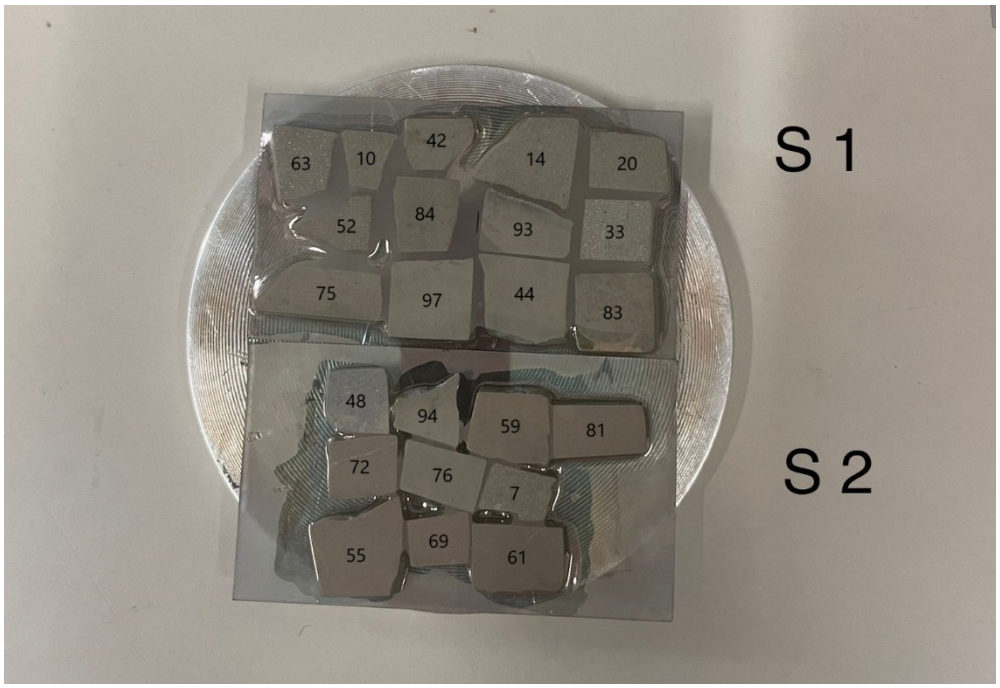

Figure 9. The final shape of the twenty-three etched samples mounted on slides S1 & S2.

Figure 10. The Elmasonic ultrasonic cleaner is used in order to remove the contaminants from the etched samples.

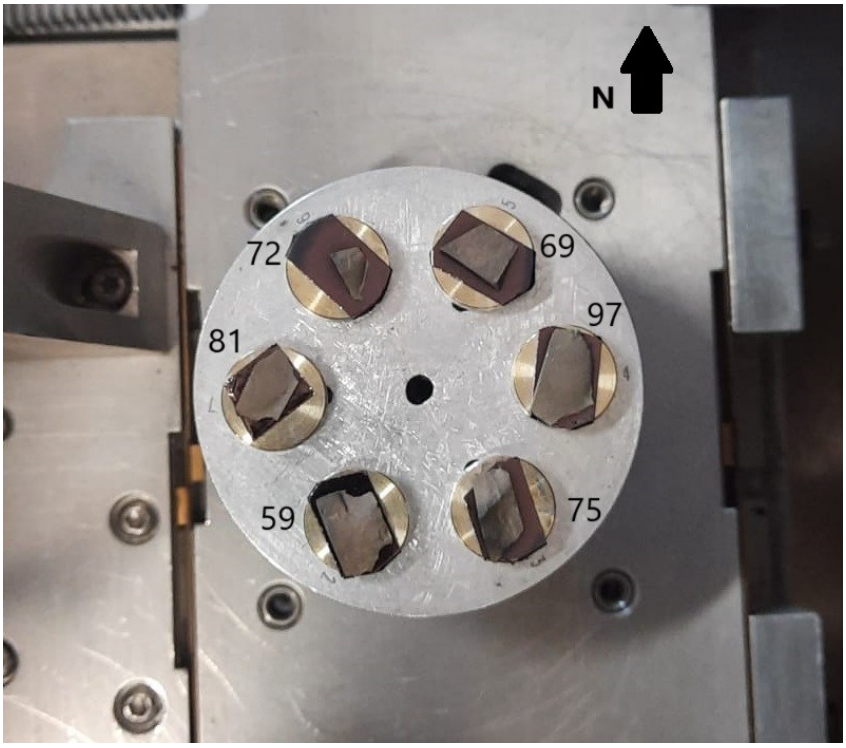

Figure 11. The final shape of the gold-coated samples.

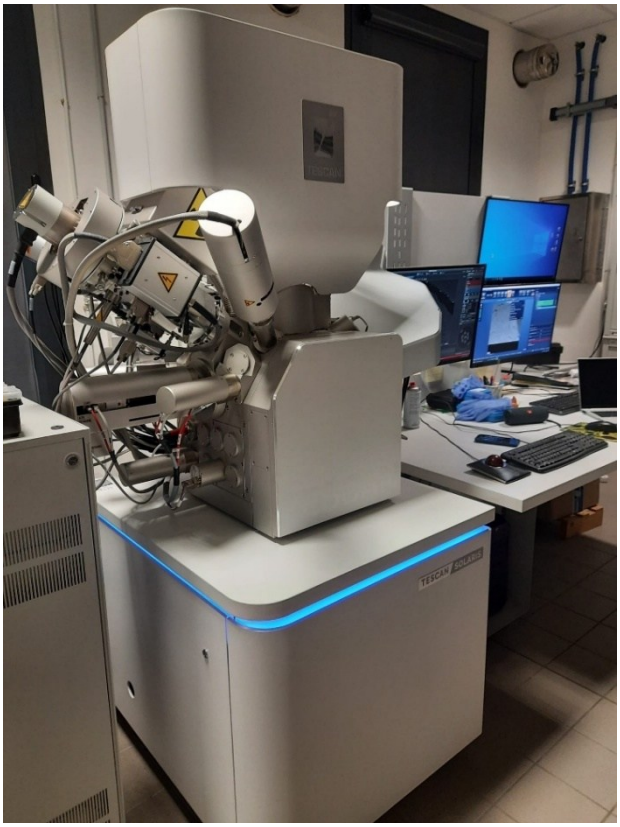

Figure 12. Zeiss EVO LS 10 Scanning Electron Microscope (SEM) was used during the analysis at the Department of Geosciences, University of Padova.

2.4. Quantitative petrography

Out of the 31 thin sections, 14 were chosen for the quantitative petrographic study of ooids according to the abundance and clarity of the ooids in the sections.

Ooids were manually counted and categorized based on their morphological and textural characteristics. GIMP (GNU Image Manipulation Program) was used for this process. On high-resolution photos of the thin sections, a quadrilateral grid was created to carefully encompass particular regions and prevent sampling bias. To ensure uniform inclusion criteria, every ooid inside the confined region was visually identified and counted.

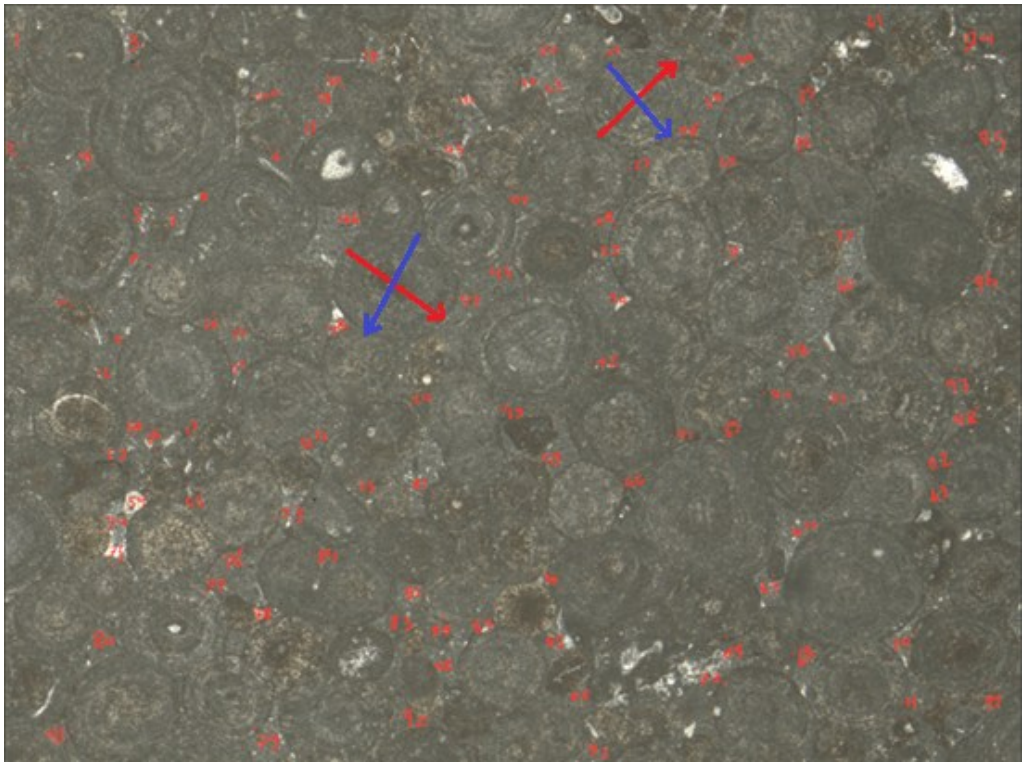

Figure 13. Part of the measurement process, the red arrow represents the major axis, and the blue arrow represents the minor axis for selected grains, sample TO 85.

For the purpose of gathering data, each sample's ooid size by measuring the long and short axes, shape, type of lamination, and mineralogical composition were annotated. Several fields of view in some samples were counted in order to guarantee statistical representativeness (Fig. 13 & 14).

The ooids' major and minor axes were measured using two-dimensional petrographic pictures. Such 2D measurements of 3D objects cannot overstate the major axis length, but they can underestimate it by as much as 35% (Howes et al., 2021). The interpretation was centered on the 50th to 100th percentiles of the size distribution for each sample in order to enhance the impact of underestimating ooid size while working from petrographic pictures (Koeshidayatullah et al., 2022).

So, overall, the study dataset used in this investigation includes the measurement of the ooid size by measuring the long and short axes and measuring its different percentile (100th, 95th, 75th,..) and the mean. Also the occurrence of the typical-sized ooid (≤1000 µm), giant ooids (>2000 µm), next to shape, type of lamination, and mineralogical composition were noted. Then box plots were made to represent the size of the ooids.

Finally, To create a thorough model of ooid generation and its connection to changes in carbonate chemistry during the Aragonite Sea II to Calcite Sea II transition, the quantitative petrography results have been integrated with facies analysis and isotopic data.

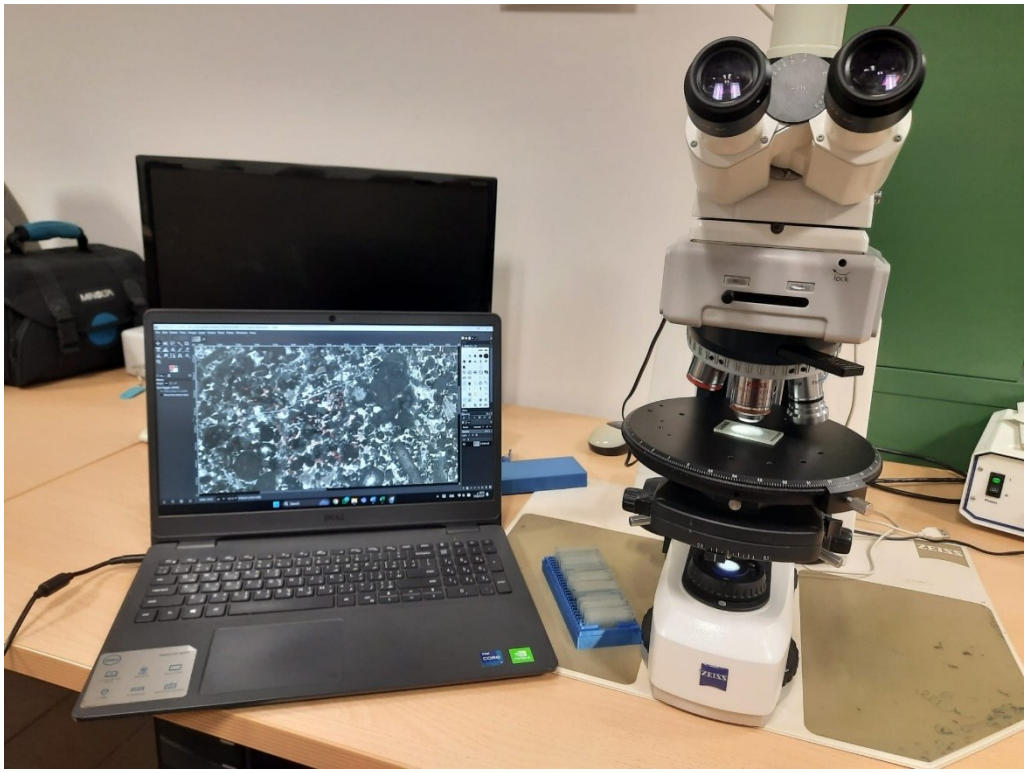

Figure 14. Part of the mineralogical analysis process for the ooids.

3. Results

3.1. Log and facies analysis

This section presents the results of the stratigraphic log and facies analysis by integrating field observations, thin-section petrography, and sedimentological data to identify depositional environments, characterize carbonate facies, and refine the stratigraphic framework of the studied sequence and its age. The section is described with reference to members of Fonzaso Fm. defined by Picotti and Cobianchi (2017).

3. 1. 1. The Lower Oolitic Member

The stratigraphic log (Fig. 17) reveals a succession primarily composed of oolitic limestones, with variations in facies that correspond to distinct depositional settings. The lower portion of the log, from its base to the fine limestone layer associated with sample TO 44, is dominated by medium- to thick-bedded calciturbidites of oolitic grainstone. These calciturbidites exhibit fining-upward trends in some sections, indicative of episodic turbidity currents. Such currents transported sediment downslope, forming graded bedding. This pattern suggests deposition during high-energy events followed by quiescent intervals, as evidenced by faint laminations observed near sample TO 19.

Dolomitization is pervasive in this interval, with variable intensity. For instance, sample TO 28 exhibits dolomitized zones accompanied by chert nodules, while samples TO 25, TO 30, and TO 33 show heavy recrystallization. Notably, sample TO 02 also displays dolomitization, although in discrete isolated crystals distributed throughout the sample (Fig. 15). Thin-section analysis confirms a dominance of grainstone textures (e.g., TO 02, TO 03, TO 13, TO 16), interspersed with small portions of packstone containing significant amounts of ooids alongside bivalves, sponges, echinoderms, intraclasts, foraminifera, and brachiopods (e.g., TO 03, TO 13, TO 16; Fig. 16). In contrast, sample TO 42 stands out as a wackestone with radiolaria grains and occasional veins. These observations align with the characteristics of the Lower Oolitic Member of the Fonzaso Formation which spans from the Upper Bathonian to the Lower Oxfordian, as supported

by nannofossil dating (discussed in detail later). The thickness of this interval is estimated at approximately 53.7 meters.

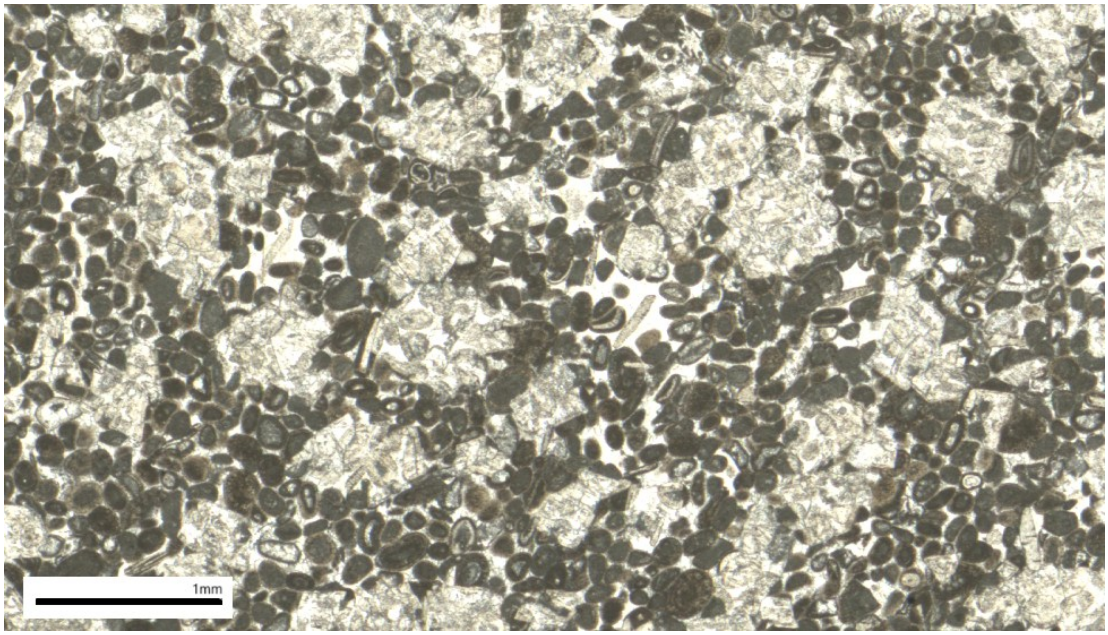

Figure 15. Fine-grained oolitic grainstone that was partially dolomitized. Dolomite appears in isolated crystals with rhombic sections, within which the grains of the original rock are still visible as ghosts, sample TO 02, the photo was taken by a slide scanner.

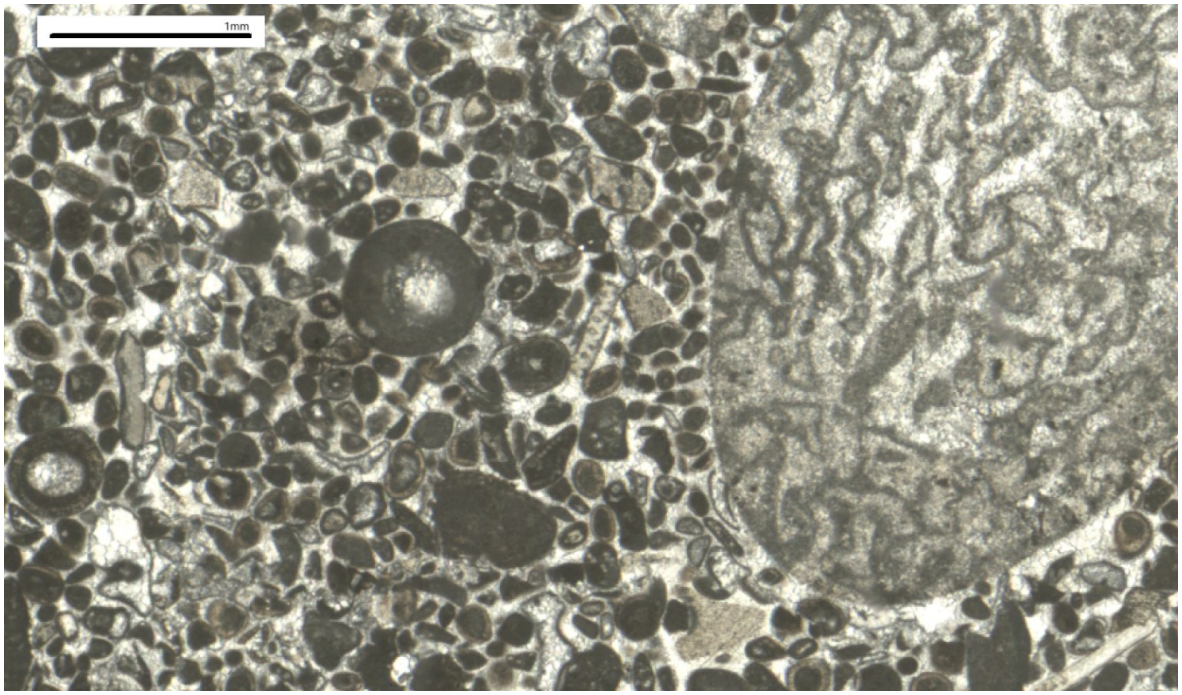

Figure 16. Oolitic packstone with a big sponge on the right side of the section, radial, micritic ooids, and small fragments of echinoderms, sample TO 13, the photo was taken by a slide scanner.

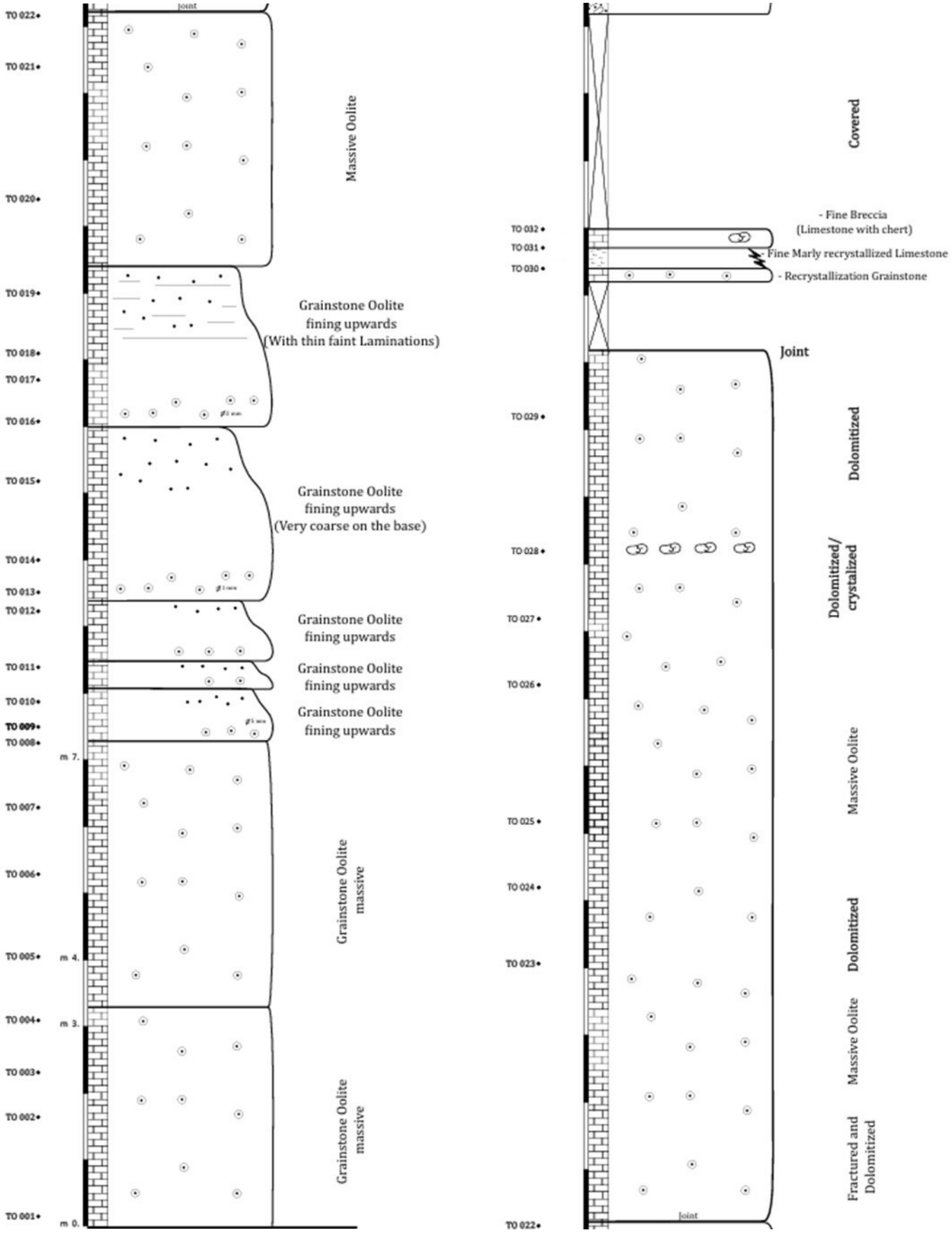

Figure 17. Stratigraphic log of the studied section, illustrating the vertical facies variations.

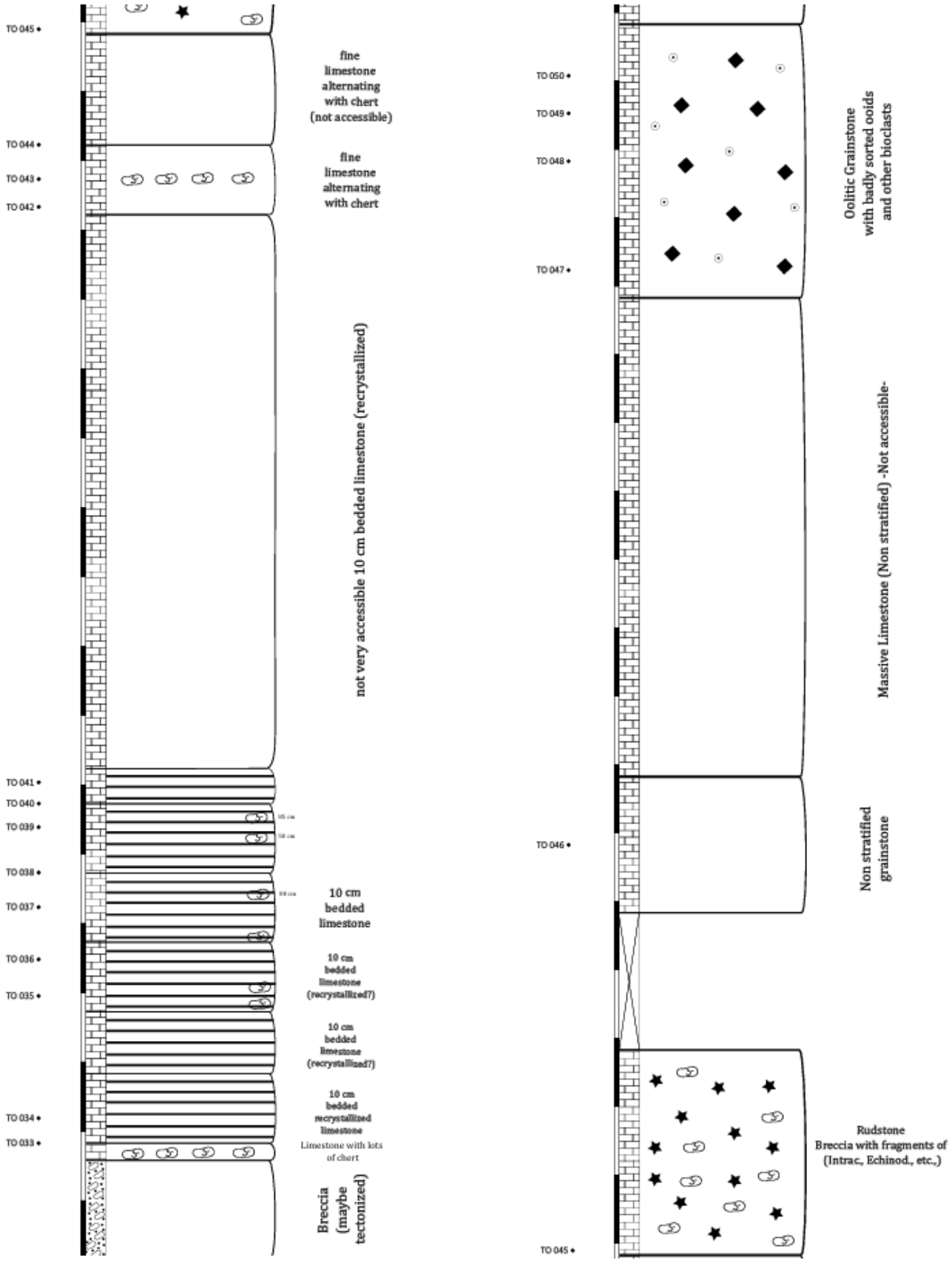

Figure 17. (*continued*).

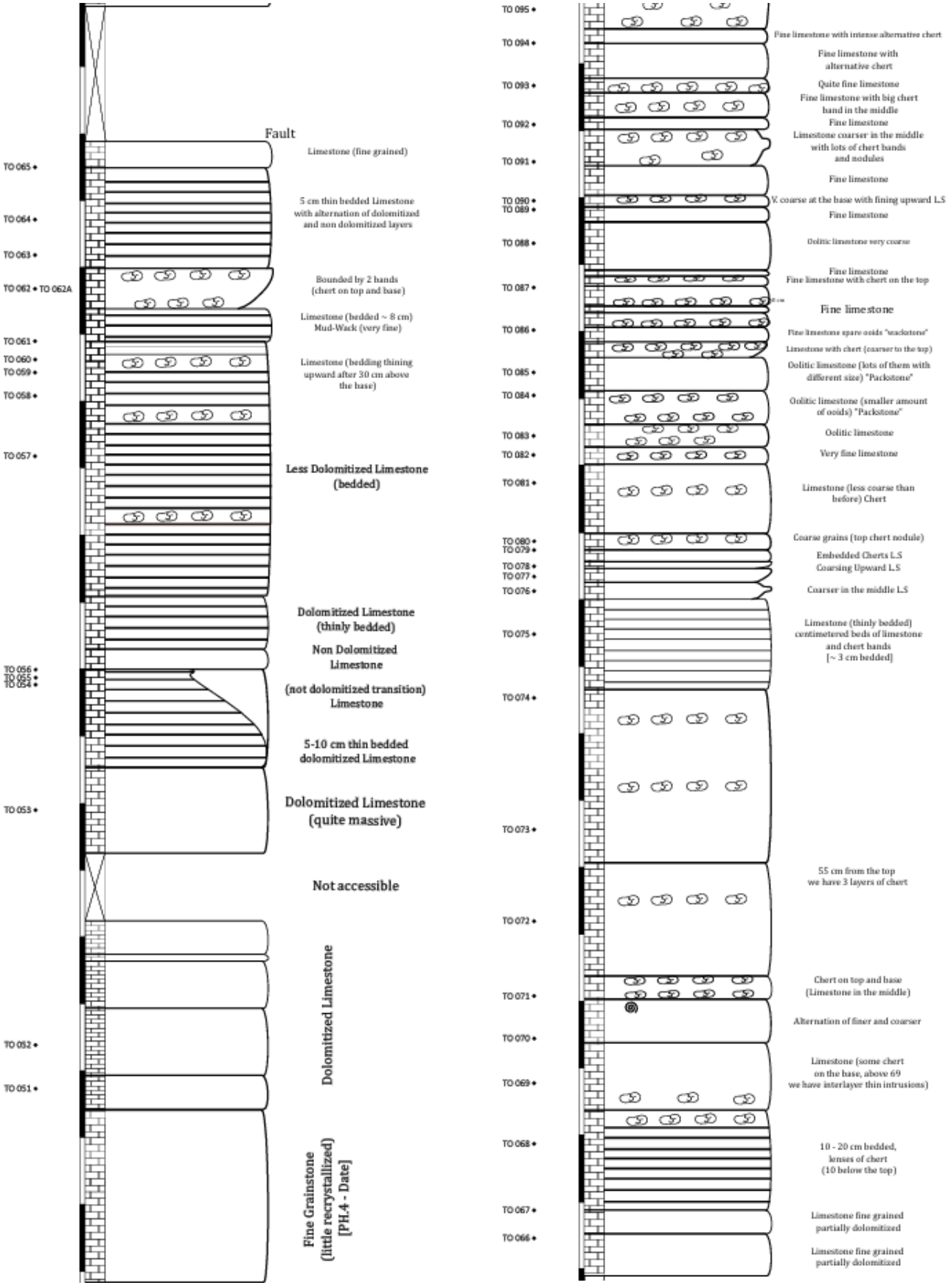

Figure 17. (continued).

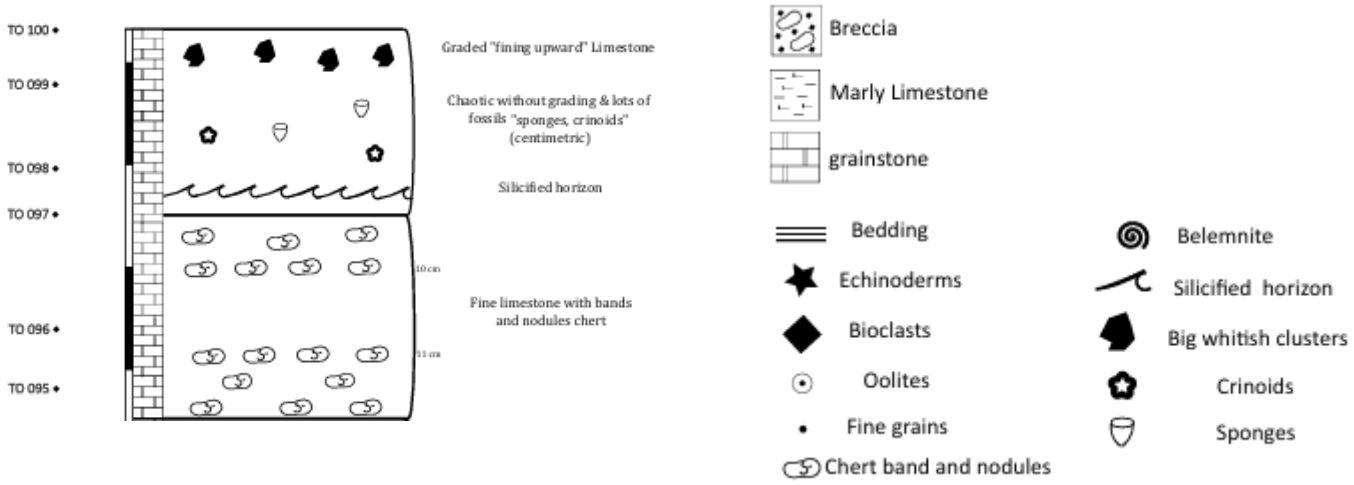

Figure 17. (*continued*).

3. 1. 2. The Skeletal Member and its transition layer

The transition from the oolitic to the skeletal member is marked by a breccia layer supported by a bioclastic matrix, characterized as rudstone breccia containing fragments of intraclasts, echinoderms, and other bioclasts (sample TO 45; Fig. 17). This breccia layer, approximately 3 meters thick, serves as the classical marker for the onset of the Skeletal Member (Picotti & Cobianchi 2017). Thin-section analysis of samples TO 45A and TO 45B reveals a diverse assemblage of calcareous sponges, calcareous algae, ooids, oncoids, brachiopods, foraminifera, echinoderms, corals, microbial micrites, and *Cayeuxia* (Fig. 18).

An earlier breccia layer, approximately 1.5 meters thick, is also noted in the previous part of the section. However, this layer, likely of tectonic origin, is nearly devoid of fossil content, distinguishing it from the bioclastic breccia.

Coinciding with the literature, this interval is overlain by bioclastic grainstones, represented by the layers encompassing samples TO 46 to TO 57. Above this, the succession transitions into a middle part dominated by dolomitized limestone. This is followed by a thinning-upward succession of light grey lime mudstones interbedded with marly layers. Throughout the whole member, there is an abundance of chert nodules and ribbons.

Thin-section analysis after the breccia transition reveals an initial dominance of grainstone textures (e.g., samples TO 46 and TO 49). However, cementation begins to disappear within the mud matrix from sample TO 49 onward. As the succession progresses, the facies transition to packstone and wackestone carbonate rocks, with varying amounts of ooids, oncoids, sponges, echinoderms, bivalves, intraclasts, foraminifera, brachiopods, and microbial micrite. Fine-grained facies are rich in radiolaria. Radiolaria are particularly abundant in samples TO 57, TO 93, and TO 95, where they completely fill the thin sections, with notable concentrations in samples TO 62A and TO 83 (Fig. 19) and lesser occurrences in samples TO 78 and TO 90.

Notably, in many thin sections, cementation is significantly reduced, leading to an increase in mud content. As a result, these samples exhibit a transition from grainstone to

a muddier texture. However, localized occurrences of cement alongside mud are still observed in samples TO 85, TO 88, and TO 90.

This member, including the breccia transition, has a cumulative thickness of approximately 58 meters and it is represented on the log from the sample (TO 45) to (TO 96); (fig. 17).

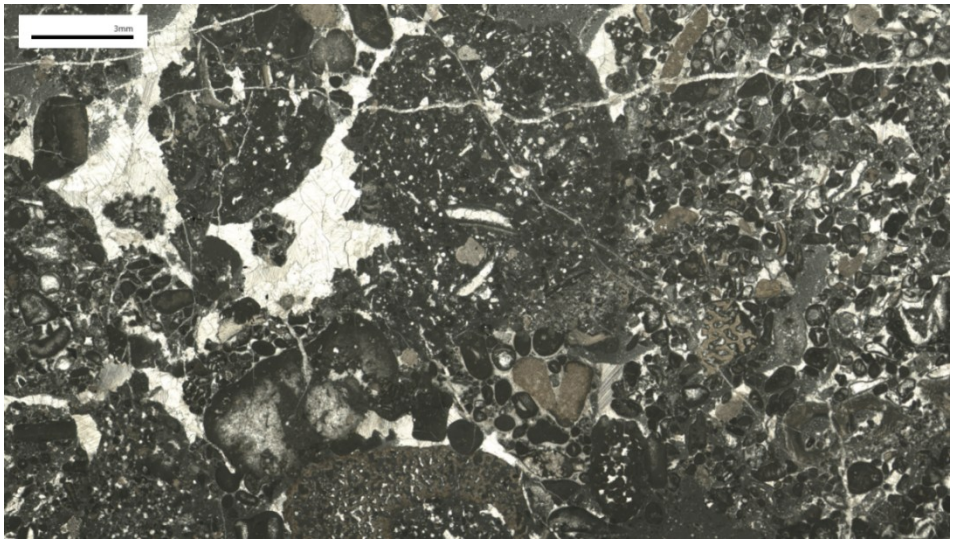

Figure 18. Rudstone-breccia, showing a coarse-grained fabric composed of angular to subangular lithoclasts and bioclasts within a dark micritic matrix. The smaller grains include peloids, ooids, and skeletal fragments in addition to different types of sponges. Bright regions correspond to calcite cement, sample TO 45 A, the photo was taken by a slide scanner.

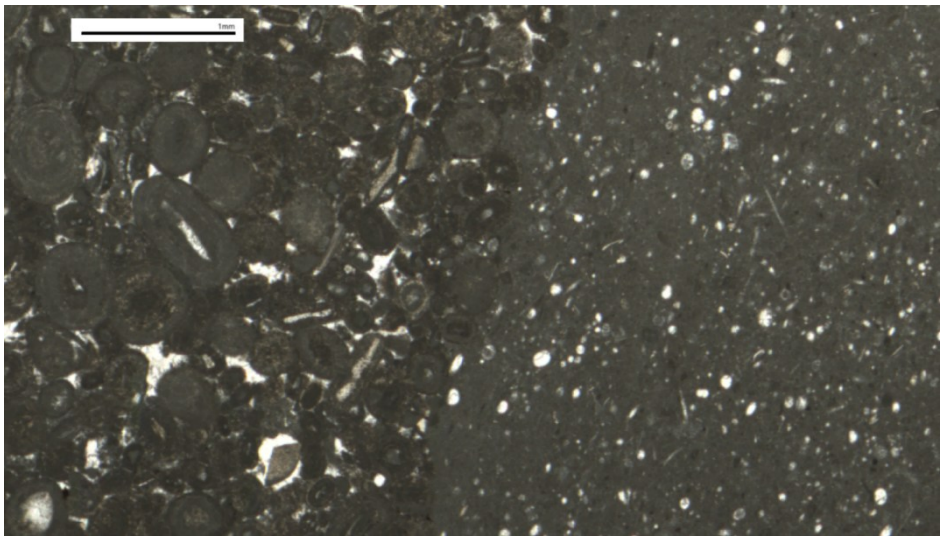

Figure 19. A sharp lithological boundary between an ooid-rich grainstone (left) and a fine-grained micritic wackestone (right). The grainstone is composed basically of ooids, while the wackestone consists of a fine-grained micrite matrix with dispersed skeletal fragments and radiolaria, sample TO 83, the photo was taken by a slide scanner.

The uppermost section of the stratigraphic log could represent the younger age section for the skeletal member, with less than 2 meters thick, and is distinguished by its crinoid enrichment (Fig. 20). Additional components include sponges, silicified horizons, and conspicuous whitish clusters (Fig. 17). Thin-section analysis reveals grainstone to packstone textures, featuring radial, and micritic ooids (e.g., samples TO 99, TO 100), alongside echinoderms, brachiopods, gastropods, oncoids, foraminifera, and intraclasts. Radiolaria is abundant, particularly in samples TO 98, TO 98A, and TO 99 (Fig. 21). However, we couldn't find any Saccocoma crinoids that serve as key markers of the Kimmeridgian Tithonian interval and the nodular member of the Fonzaso Fm.

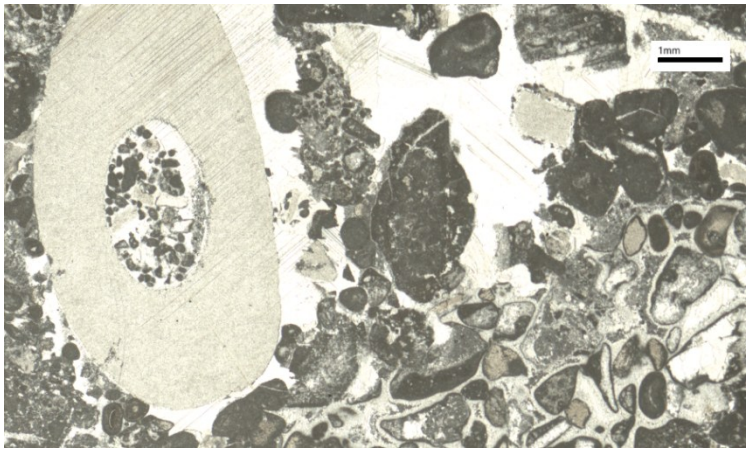

Figure 20. Coarse-grained carbonate deposit with a variety of well-preserved large coated grain (likely an ooid or oncoid) with a big crinoid on the left. The surrounding matrix is composed of intraclasts, bioclasts, and peloids, with some areas displaying sparry calcite cement, sample TO 89 A, the photo was taken by a slide scanner.

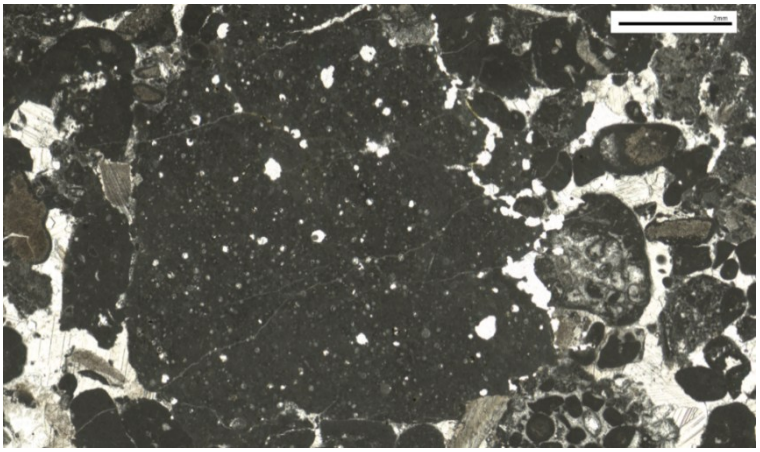

Figure 21. Carbonate breccia with a large micrite-filled cavity in the center, with abundant radiolaria. The surrounding clasts consist of various carbonate components, including bioclasts, peloids, and intraclasts, bound by sparry calcite cement, sample TO 99, the photo was taken by a slide scanner.

3.2. Stable isotopes

The $\delta^{13}C$ values generally range from -6.10 to +4.03 ‰ (mean +1.95‰) (Fig. 22), and $\delta^{18}O$ from -10.02 to -0.14 ‰VPDB (mean -3.13 ‰). In the cross-plot, most data points show a direct correlation between $\delta^{13}C$ and $\delta^{18}O$, i.e., samples with lower $\delta^{18}O$ tend also to have lower $\delta^{13}C$. This is typical of burial diagenesis, and it is quite normal to find it in a series of Mesozoic bulk samples. Here, we have $\delta^{18}O$ values that reach as low as -10‰ while normal marine values would be at around 0 to -2 ‰.

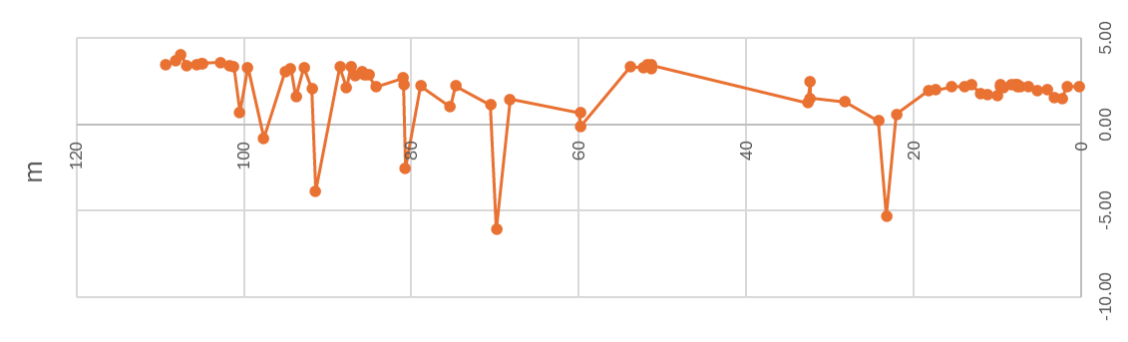

Figure 22. Distribution of δ¹³C (‰ VPDB) in bulk samples as a function of distance interval, plotted against log data for the entire section.

The lower the $\delta^{18}O$, the deeper burial cements are in the sample, because these cements form deep in the crust, at high T, and hence have lower $\delta^{18}O$. They have lower $\delta^{13}C$ because, possibly, organic matter in the sediment was converted into CO_2 by respiration during burial, that CO_2 mixed with that of dissolving $CaCO_3$ (e.g., from the aragonite components of the sediment), and was then incorporated in late burial cement. CO_2 from respiration is very negative in $\delta^{13}C$, and hence, it drags down the $\delta^{13}C$ of bulk carbonate if incorporated in it. And while burial diagenesis is a localized process, it has not been commonly recorded in regional studies.

If this was the case, the most reliable samples are those with less negative $\delta^{18}O$, which contain less carbonate formed at high T. So we set an arbitrary cutoff at a $\delta^{18}O$ of -5‰, and discard all samples below it. The remaining samples should be more likely to be pristine (Fig. 23). Like that 14 samples will be cut off from the calculation and the $\delta^{13}C$

values will range from -0.81 to +4.03 ‰ (mean +2.51‰), and $\delta^{18}O$ from -4.45 to -0.14 ‰VPDB (mean -2.29‰) (Fig. 24).

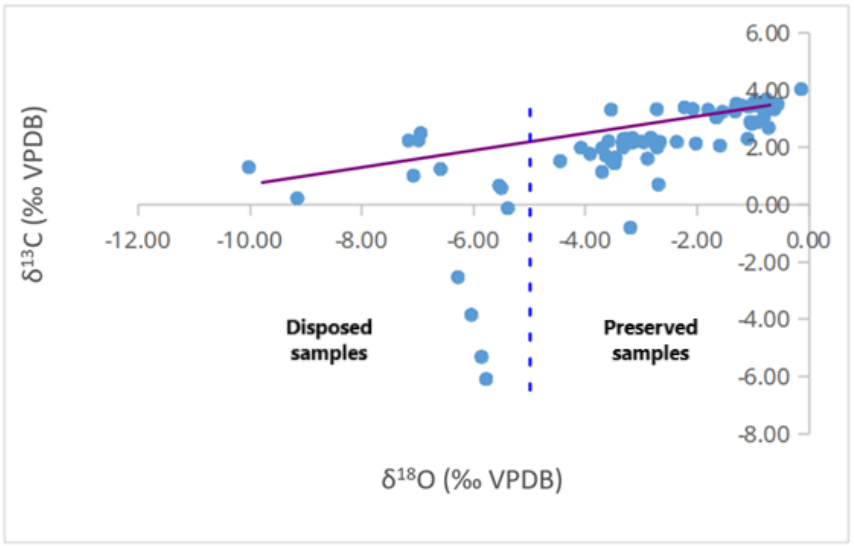

Figure 23. Stable carbon- vs. oxygen-isotope cross-plot of the bulk studied samples with the cutoff threshold.

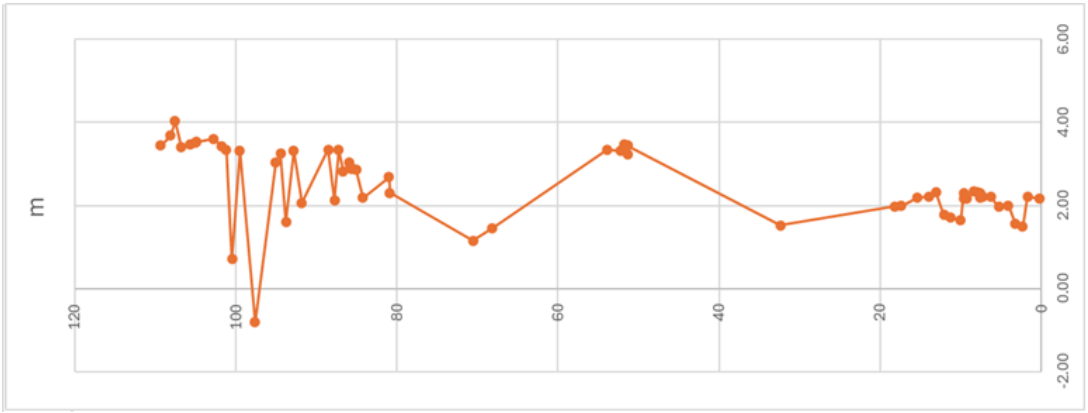

Figure 24. Distribution of $\delta^{13}C$ (‰VPDB) for the bulk samples as a function of distance interval, plotted against log data after the cutoff process.

Like that, the $\delta^{13}C$ values more or less coincide with the isotopic values of The Adriatic Carbonate Platform, Croatia where $\delta^{13}C$ values generally range from -1.8 to +4‰ (mean +1.9‰), and $\delta^{18}O$ from -3.5 to +3.1‰VPDB (mean 1.1‰) during the Oxfordian and the Kimmeridgian periods (Fig. 25 & 26; Husinec, A., et al 2022), which align with the approximate dating which was detected also from the log analysis results according to the Fonzaso FM., But overall, in contrary to it, as it is clear from the graph, there aren't any

positive values for the $\delta^{18}O$ from our studied samples. So in general, we hope that we will be able to find a correlation between them.

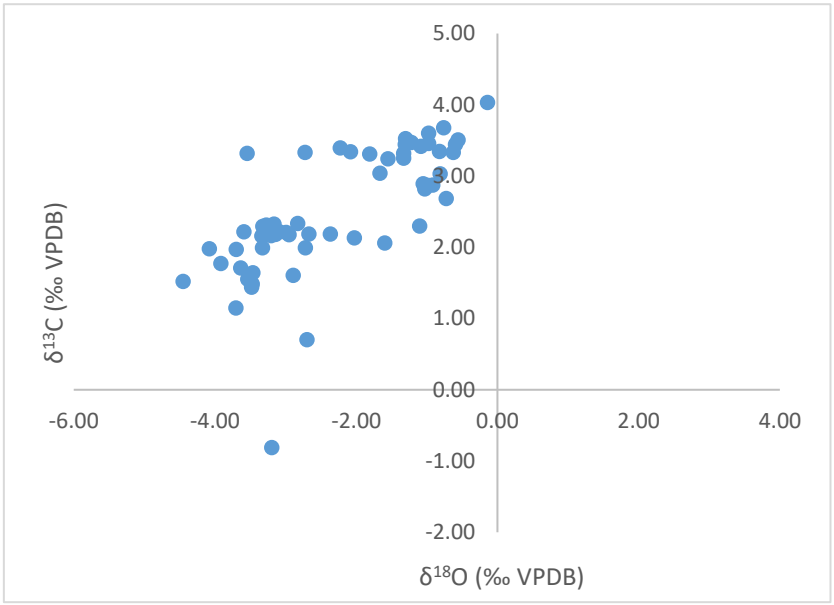

Figure 25. Stable carbon- vs. oxygen-isotope cross-plot of the studied samples after the cutoff process.

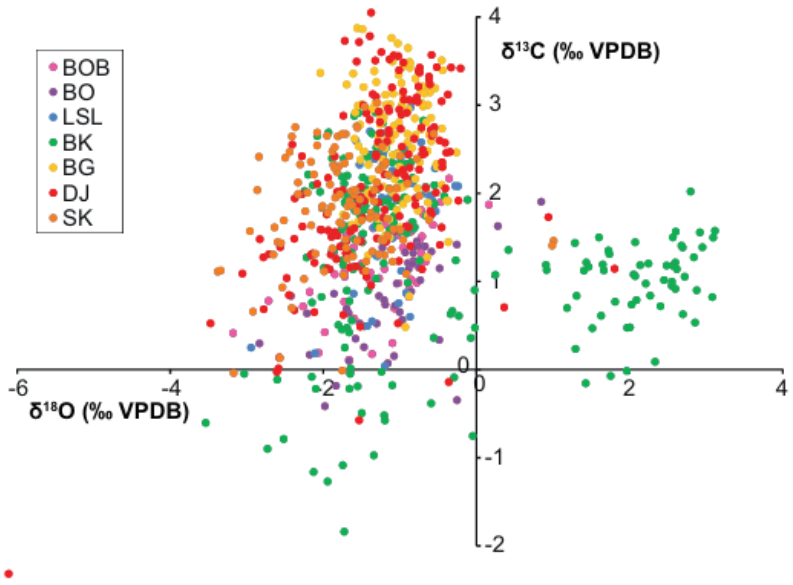

Figure 26. Stable carbon- vs. oxygen-isotope cross-plot of samples from the composite middle Bajocian-basal Berriasian section, Adriatic platform, Croatia. (upper Tithonian-lower Berriasian: sections BO and BOB, Brotnice Obić), (Tithonian-lower Berriasian: section LSL, Lastovo Island),(late Oxfordian-early Tithonian: section BG-BK, Brotnice), (upper Callovian-Oxfordian-lower Kimmeridgian: section DJ, Dubrovnik-Jasenice), and (upper Bajocian-Bathonian-lower Callovian: section SK, Smrekovo Korito) (Husinec, A., et al 2022).

3. 2. 1. Oxfordian age

The $\delta^{13}C$ values of bulk carbonate limestone from the first section which can be a part of the Oxfordian (according to the predictable period from the log and the SEM results), range from +1.15‰ to +3.46‰ (mean +2.35‰) (Fig. 27 & 30), but in the case of leaving the original values before the cut-off, we will have nearly the same range but with just three values from 0 to +1‰ out of 46 samples (two from Lower-middle Oxfordian and one from the Late Oxfordian section) and four samples with negative excursions from 0 to -6‰. However, the $\delta^{18}O$ values range from -4.45 to -0.72 ‰VPDB (mean -2.61‰).

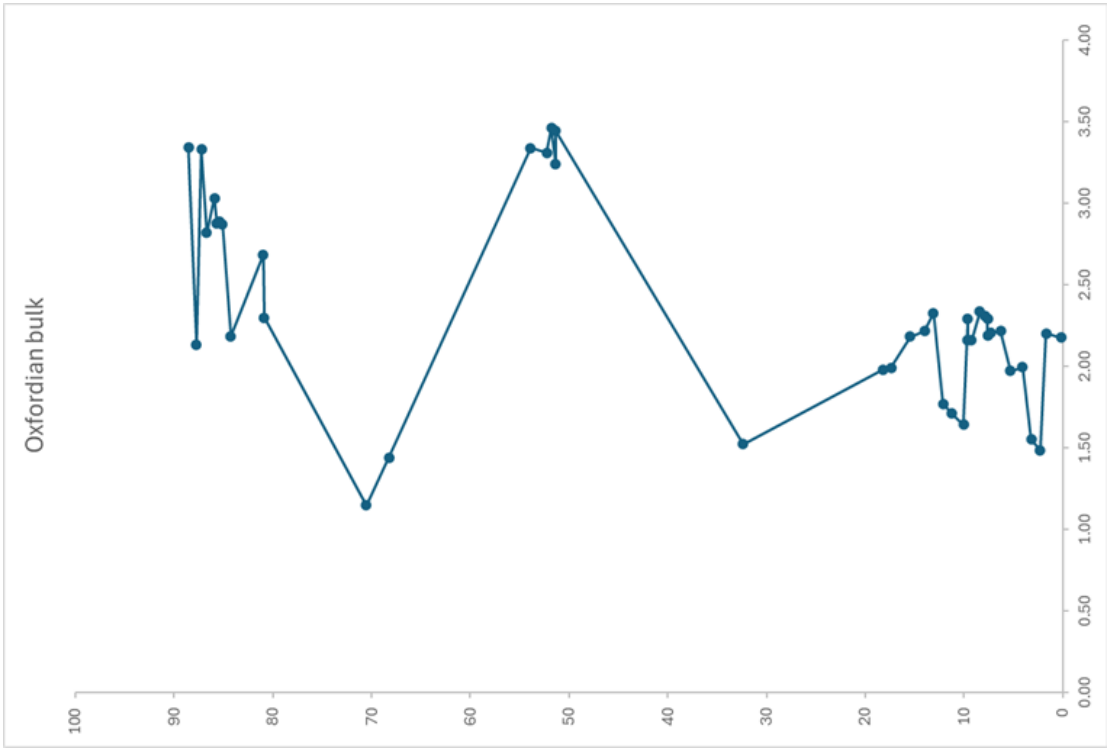

Figure 27. The $\delta^{13}C$ (‰VPDB) data after the cutoff for the bulk samples of the Oxfordian section.

While we can find the $\delta^{13}C$ values of the Upper Callovian-Oxfordian-basal Kimmeridgian DJ section (Dubrovnik Jasenice) in the Adriatic Carbonate Platform, Croatia, which is introduced here because it covers these two stages, and we wish to attempt to make a correlation with it. The Oxfordian section in the study generally ranges from -2.3 to +4‰ (mean +2.1‰) (Fig. 28), and $\delta^{18}O$ from -3.5 to +1.8‰VPDB (mean 1.3‰). The bulk of the DJ section (0–298 m) is characterized by a stepwise increase in $\delta^{13}C$ values, which is interrupted by a major negative excursion to -2.3‰ at 135 m, and two minor negative excursions to 0‰ at 69 m, and +1.6‰ at 232 m. The remainder of the section shows

gradually decreasing $\delta^{13}C$ values with a minimum of +1.13‰ at 324 m (Husinec, A., et al 2022).

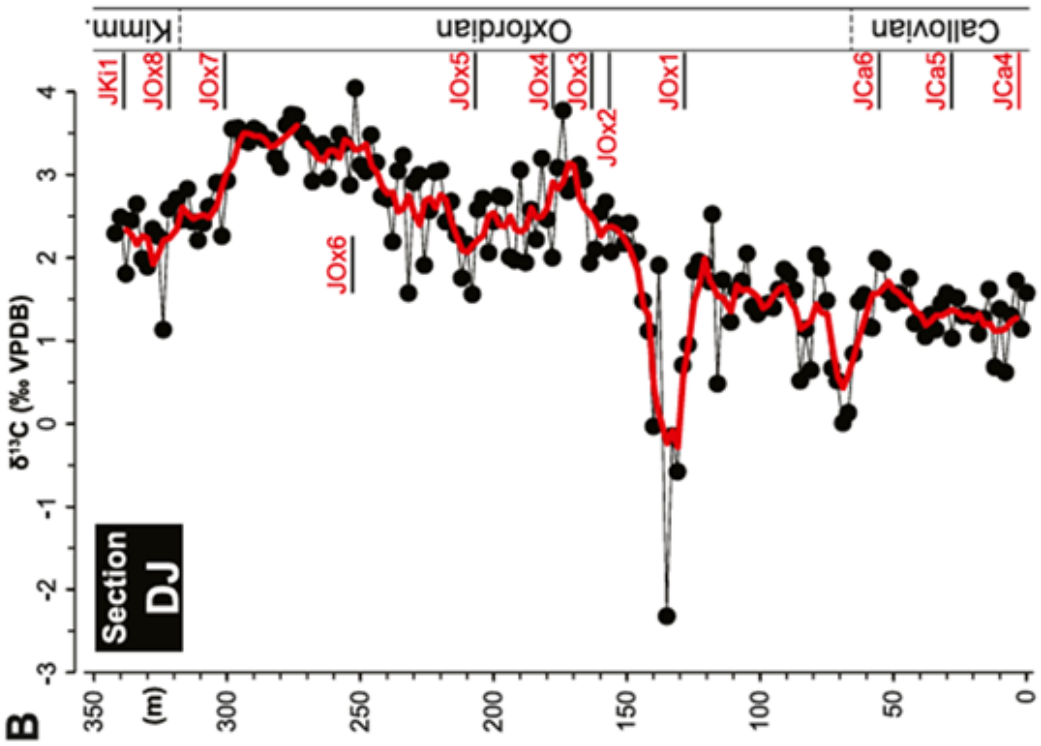

Figure 28. Carbon isotope stratigraphy vs. thickness of the Callovian-Oxfordian-Kimmeridgian section of the Adriatic platform. The thick red line indicates 3-point moving average. (B) Section Dubrovnik Jasenice (Husinec, A., et al 2022).

In our section we nearly have more than 90 m in thickness nevertheless, it is not known for certain the upper or the lower boundary of the Oxfordian age, which is the upper one defined here by a progressive rise in $\delta^{13}C$ values, broken up by a huge negative excursion to -5.32‰ at 23.25 m, as well as two minor negative excursions next to it, to +0.58‰ at 22.1 m and +0.22‰ at 24.2 m "before the cut-off" next another two troughs that represented here in the graph (Fig. 30) to +1.52‰ and +1.15‰ at 32.4 m and 70.55 m, respectively.

Throughout the rest of the section, the $\delta^{13}C$ values gradually decrease also, but the transition here suffers from more negative values, reaching negative troughs to +0.66 at 59.85 m, +1.44‰ at 68.25 m, +1.15‰ at 70.55 m, +1.01‰ at 75.4 m. The last segment before the shifting to the Kimmeridgian age, continues the increasing trend, followed by a decrease near the boundary, in our records reaches -3.85‰ at 91.45 m for sample TO

66, which was included in the cutoff process. For that, the Oxfordian-Kimmeridgian boundary was predicted to be located here.

While uncertainties remain, the data point towards localized diagenetic conditions that may not be recorded in the regional studies, and this is the reason for the uncertain identification of the Jurassic-Kimmeridgian boundary next to the uncertainty also in the nannofossils recording.

Overall, the $\delta^{13}C$ values are generally similar to those from veins, grains, and sponges, which all were taken from the Oxfordian age (+1 to +3‰; Fig. 29), suggesting that maybe they have not been significantly reset by diagenesis, except four samples around the range (0 to -3.3‰), three of them from the veins and one from the sponges, with the fact that all the number of samples combined from veins, grains, and sponges just 18 samples, but it's important to note that some of the samples here were part before the cutoff process.

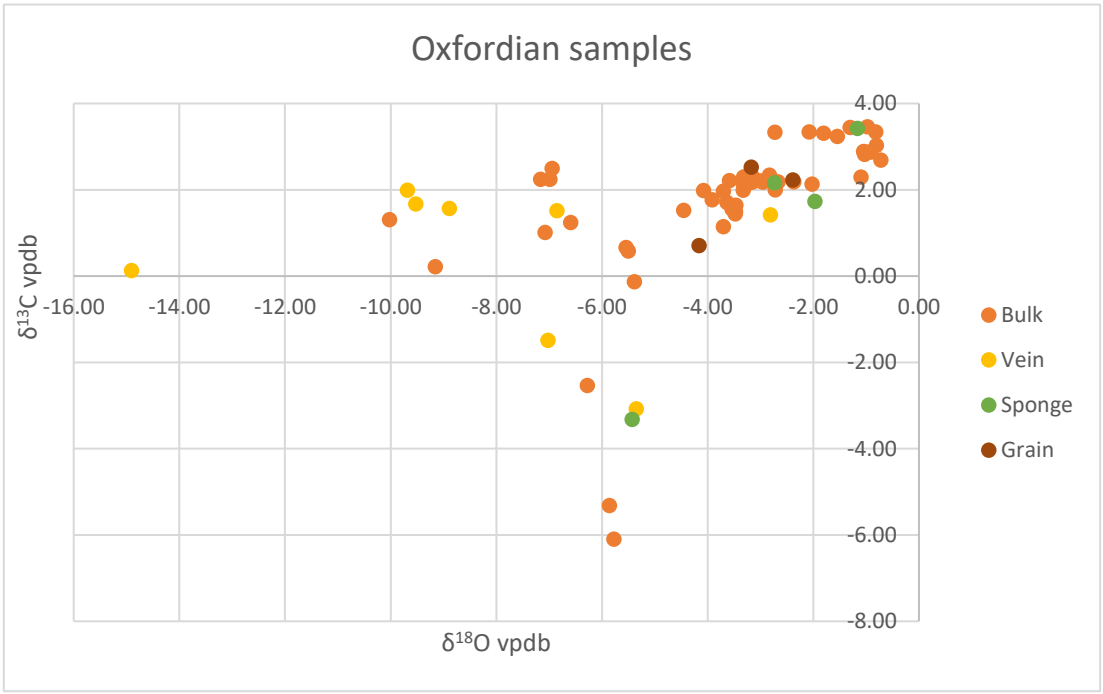

Figure 29. Stable carbon- vs. oxygen-isotope cross-plot without the cutoff processing of the bulk, vein, sponge, and grain samples.

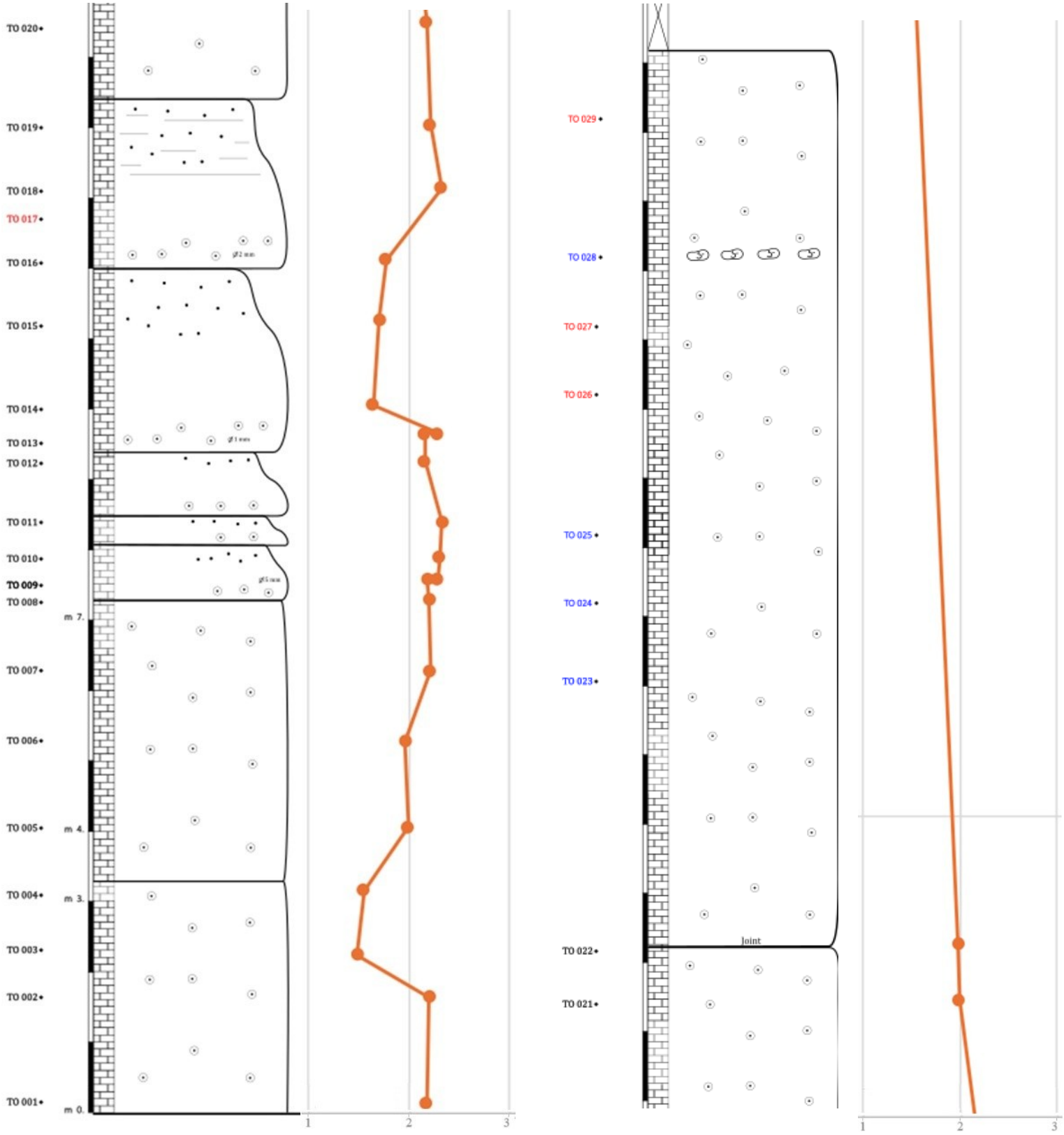

Figure 30. The Stratigraphic column of the Oxfordian section with sample numbers alongside $\delta^{13}C$ (‰VPDB) data after the cutoff for the bulk samples (The red samples: dolomites, were neglected from the beginning – The blue ones: were cut off later as was mentioned above - the missing sample numbers: were taken as just thin-section).

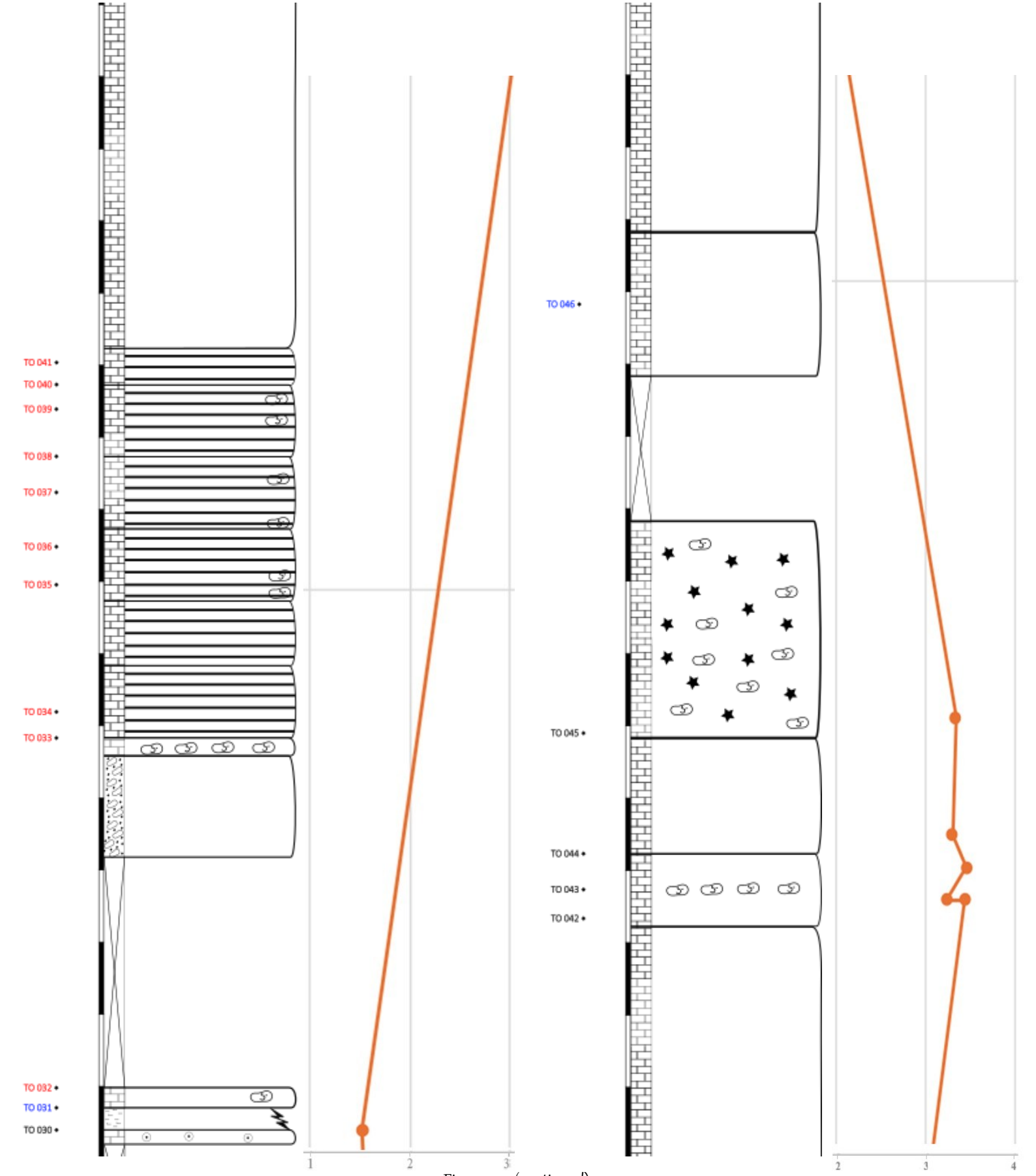

Figure 30. (continued).

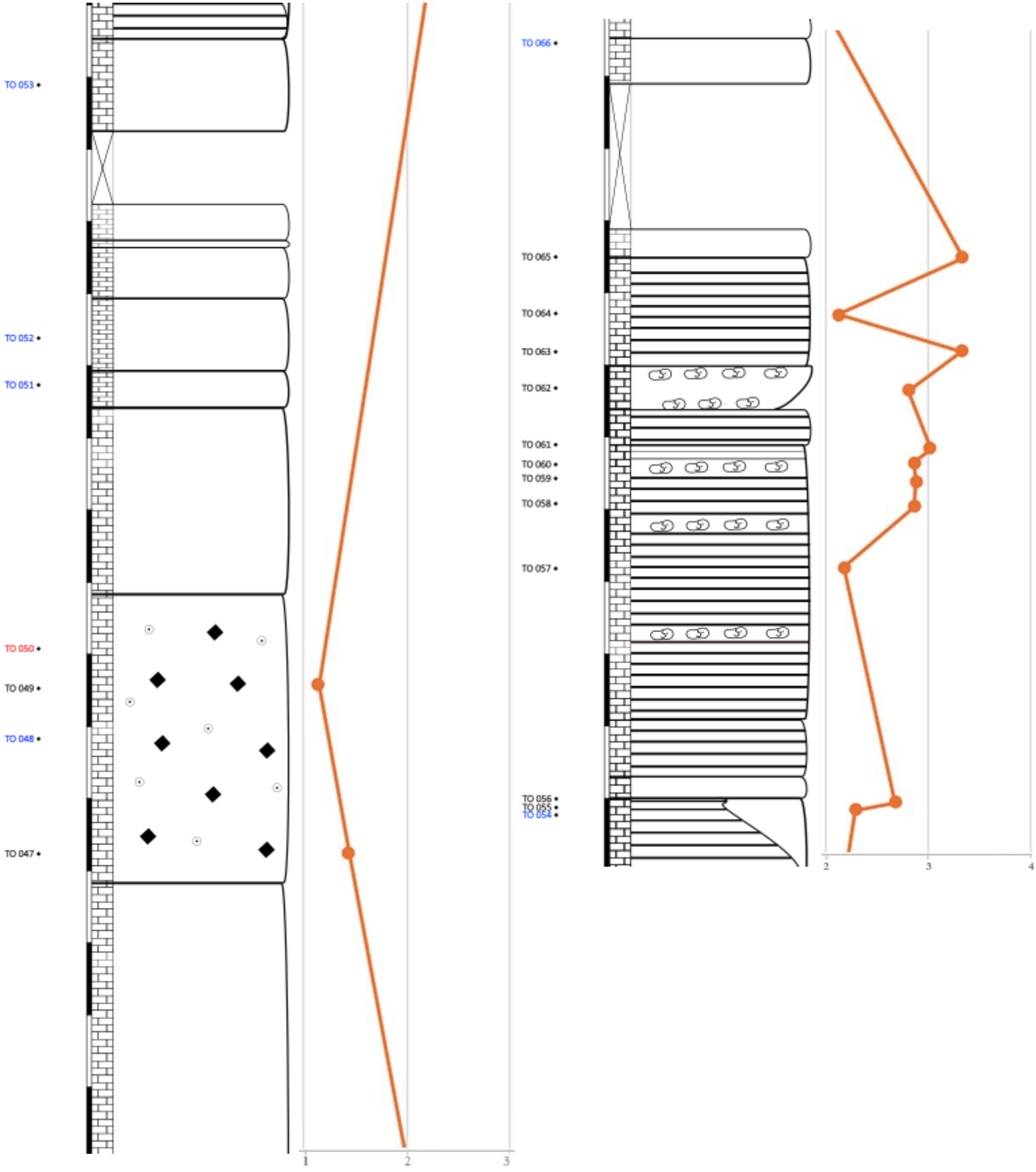

Figure 30. (continued).

3. 2. 2. Kimmeridgian age

The $\delta^{13}C$ values of bulk carbonate limestone from the Kimmeridgian mainly range from +2.06‰ to +4.03‰ (mean +2.88‰), with just two values from 0 to +1.5‰ (+0.7 & +1.60), and another one negative excursion (-0.81‰) out of 28 samples (Fig. 31 & 33). However, the $\delta^{18}O$ values range from -3.54 to -0.14 ‰VPDB (mean -1.54‰).

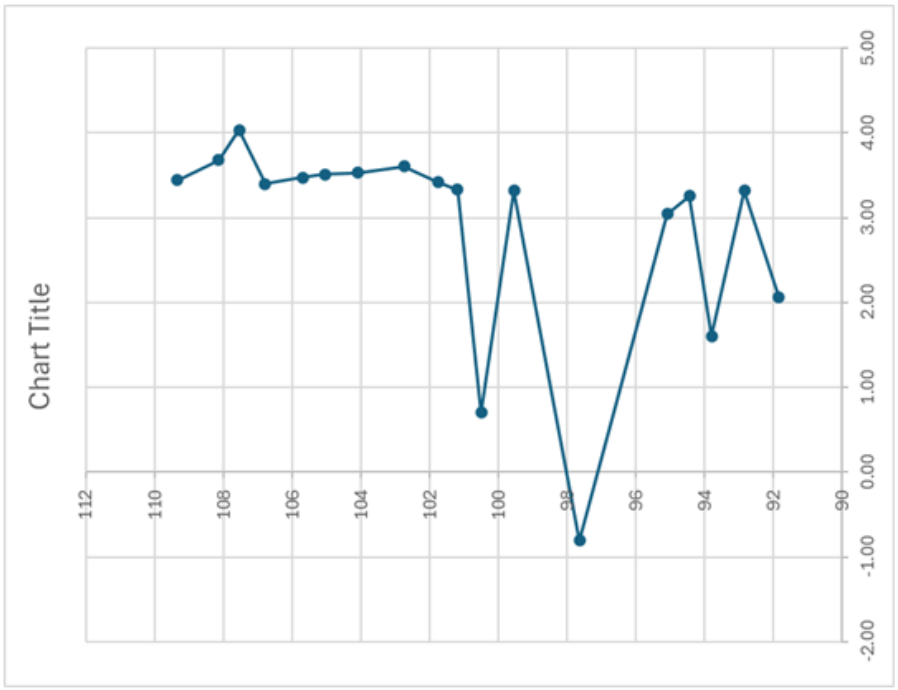

Figure 31. The $\delta^{13}C$ (‰VPDB) data after the cutoff for the bulk samples of the Kimmeridgian section.

The $\delta^{13}C$ values of the composite BG-BK section (Brotnice Gradina- Križ), according to Husinec, A., et al (2022) also, range from -1.8 to +3.9‰ (mean +1.8‰), and $\delta^{18}O$ from -3.5 to +3.1‰ (mean 0.7‰) (Fig. 32). Following a positive shift to +3.6‰, but be noticed that here the values of the section represent the values for Upper Oxfordian-Kimmeridgian -lower Tithonian. With focusing on only the Kimmeridgian $\delta^{13}C$ values, a gradual decrease is visible to +1.3‰ at 64 m, and then increases to +3.9‰ at 87 m. The remaining part of the BG section (the first part of the section, which includes the lower part of the Kimmeridgian) shows a major negative excursion reaching +0.5‰ at 127 m.

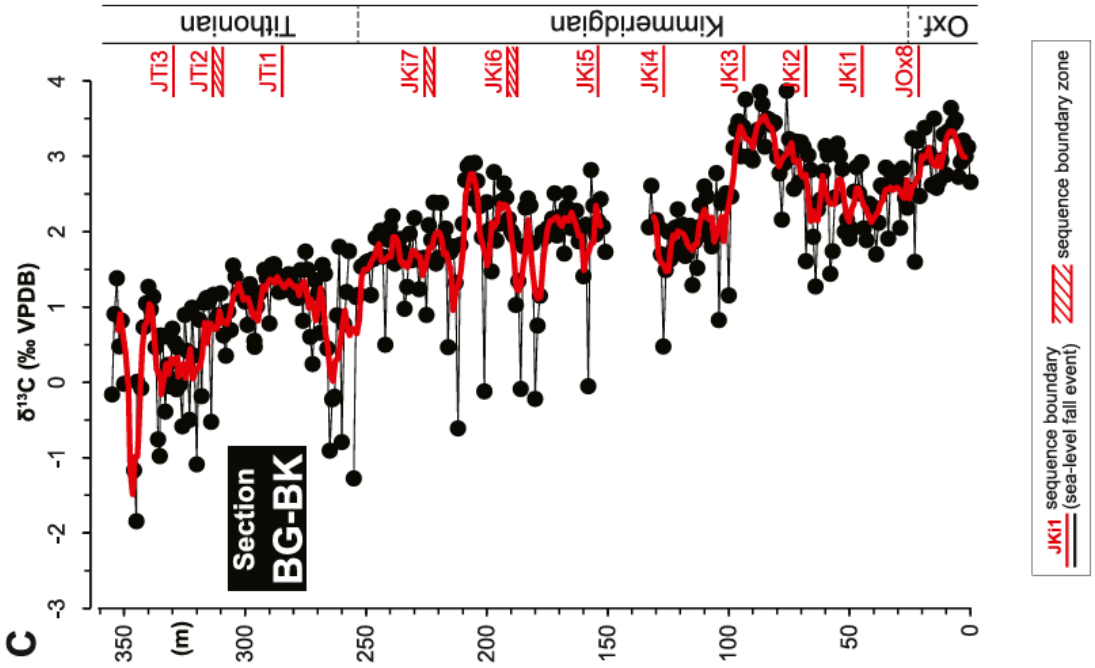

Figure 32. Carbon isotope stratigraphy vs. thickness of the Oxfordian-Kimmeridgian-Tithonian section of the Adriatic platform. The thick red line indicates a 3-point moving average. (C) Composite section Brotnice Gradina (BG) and Brotnice Kriˇz (BK) (Husinec, A., et al 2022).

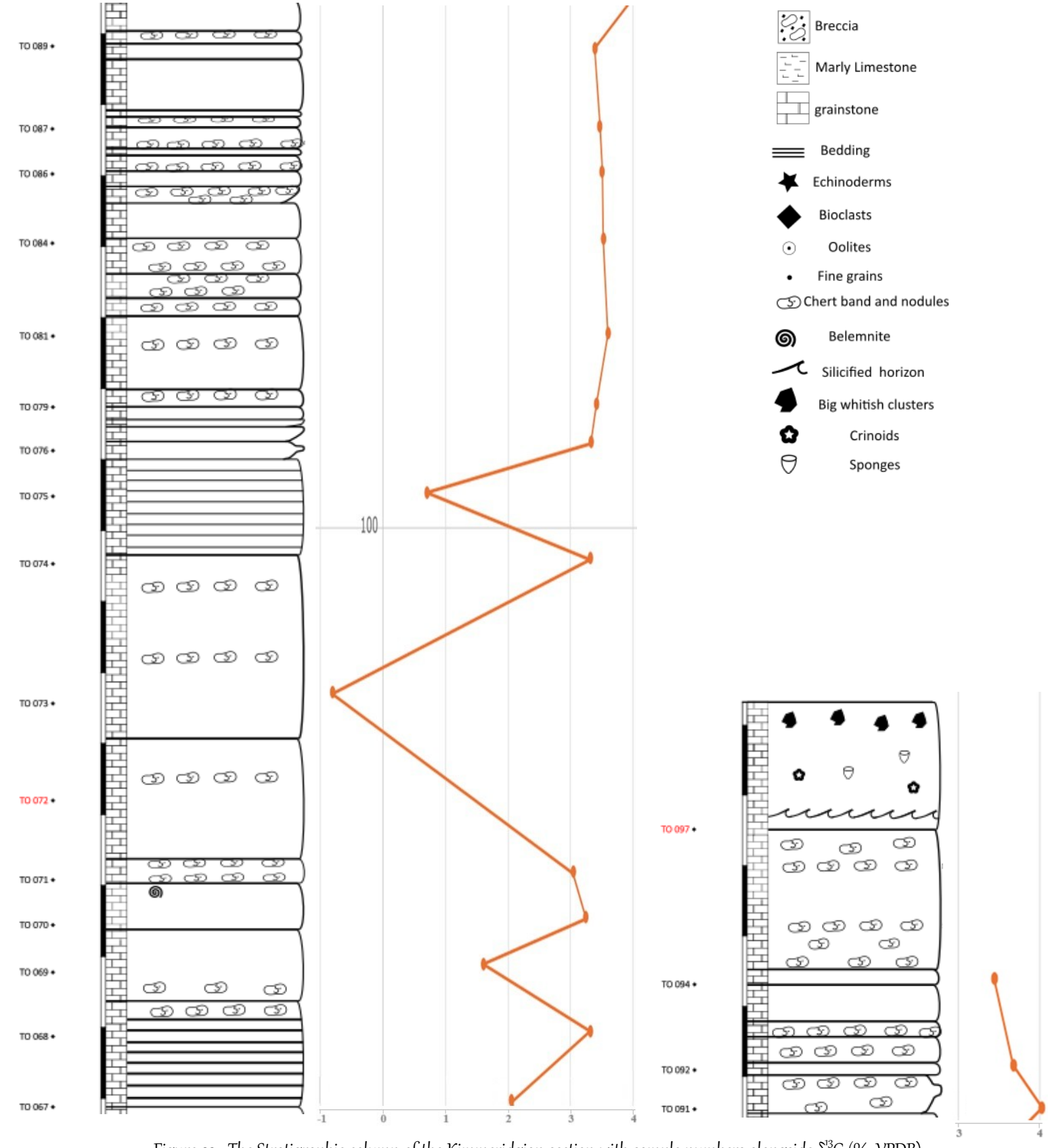

Figure 33. The Stratigraphic column of the Kimmeridgian section with sample numbers alongside $\delta^{13}C$ (‰VPDB) data for the bulk samples after the cutoff (The red samples: dolomites, were neglected from the beginning).

3.3. Nannofossil biostratigraphy

The first analysis of nannofossils in the etched samples through the whole log using Scanning Electron Microscopy at CEASC revealed several noteworthy observations (Fig. 34, 35, 36 & 37) which prompted us to use an SEM with higher resolution. As is typical with SEM studies, the observed abundance of coccoliths was relatively low compared to the results commonly obtained from smear slide preparations used in standard nannoplankton biostratigraphy. This limitation was exacerbated by the insufficient availability of material suitable for smear slide preparation in this study.

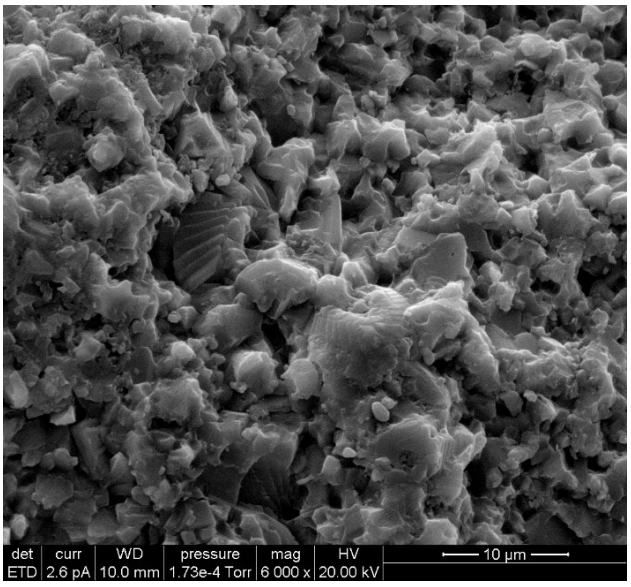

Figure 34. Different fragments of coccoliths, TO 97.

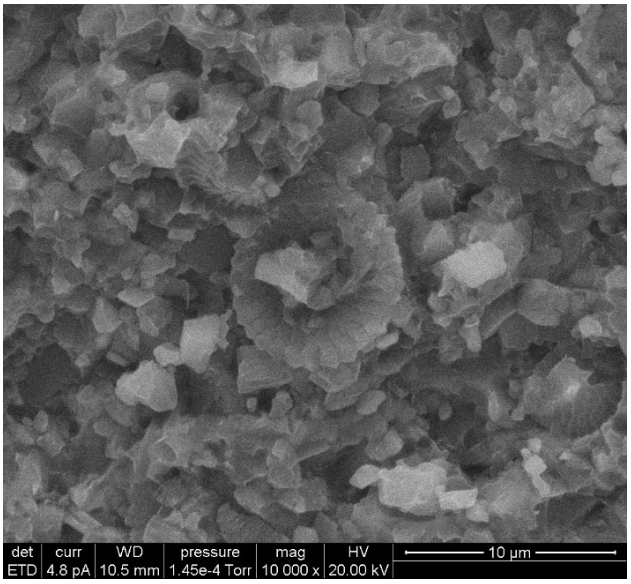

Figure 35. Coccoliths in TO 55

The low abundance of nannofossils observed in several samples is consistent with the observation that, before the Tithonian, nannofossils did not form in large amounts during the Jurassic, with preservation being particularly poor during the Callovian-Kimmeridgian interval (Casellato 2010). Furthermore, five of the 14 examined samples contained nearly no nannofossils at all, and several others had exceptionally low quantities. This scarcity aligns with the broader sedimentary patterns of the Jurassic, a period characterized by exceptionally low pelagic carbonate accumulation rates, especially in the Early and Middle Jurassic, and only widespread deposition of calcareous nannofossil oozes in the latest Jurassic (Muttoni et al., 2005). The Late Jurassic-earlier

Cretaceous interval, however, marked a crucial time in calcareous nannoplankton evolution (Casellato 2010), which could explain the modest recovery of nannofossil abundance in some of our samples.

The stratigraphic interpretation and assignment of the analyzed samples are as follows:

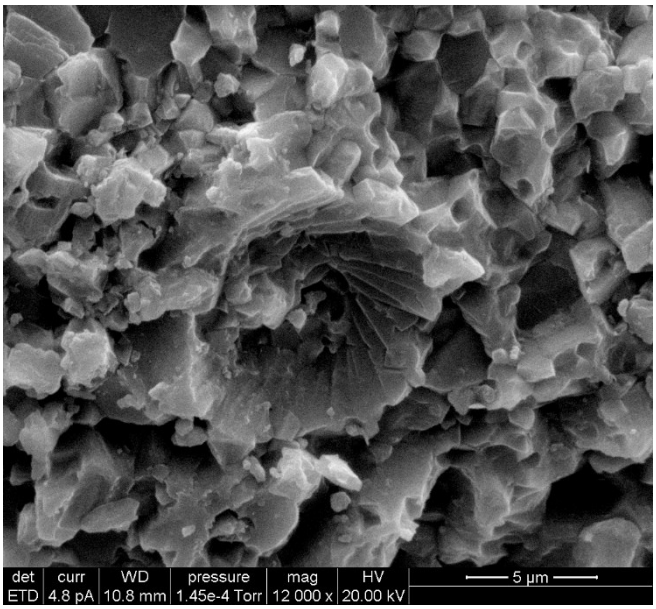

Figure 36. A coccoliths in TO 42

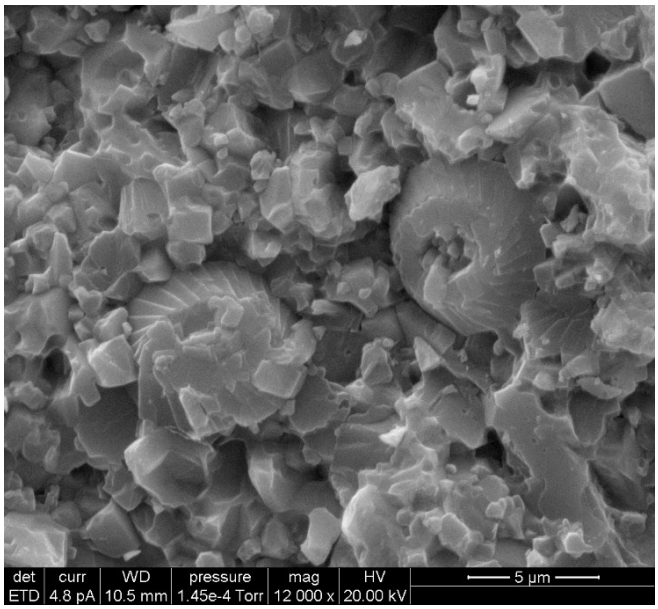

Figure 37. Side with sample TO 76.

Sample TO 42:

The sample was attributed to biozone NJT 13a as defined by Casellato (2010). This assignment is based on the presence of *Lotharingius sigillatus* (Fig. 38) in the absence of *Cyclagelosphaera wiedmannii*. Biozone NJT 13a is lower to middle Oxfordian and is dominated by associations of the genus *Watznaueria* (Chiari et al. 2007), along with the presence of *Cyclagelosphaera margerelii*,(Fig. 39) which is aligned within the sample represented by different type of *Watznaueria sp* especially *W. britannica, W. aff. W. manivitae* next to *C. margerelii,* and maybe *Biscutacean.*

Sample TO 44:

This sample exhibits an assemblage dominated by various species of the genus *Watznaueria* but lacks *Lotharingius sigillatus*. It is represented here by *W. britannica, W. fossacincta*, and *W. aff. W. manivitae (*Fig. 40*).* We have also here *Cyclagelosphaera* sp.. It is attributed to biozone NJT 13b, corresponding to the upper Oxfordian.

Sample TO 55:

Similar to sample TO044, the assemblage is dominated by *Watznaueria* species with *W. britannica* (Fig. 41) and *W. aff. W. manivitae*. It is likely attributable to biozone NJT 13b also.

Sample TO 59:

W. britannica, W. manivitae, W. aff. W. manivitae, and *W. barnesiae (Fig. 42)*

Samples TO 75 and TO 76:

These samples are challenging to assign definitively due to the observed nannofossil associations. The assemblages remain dominated by *Watznaueria* species, with the additional presence of *Triscutum*. According to Casellato (2010), *Triscutum* occurs within biozone NJT 13b, but its occurrence in biozone NJT 14 cannot be excluded. Therefore, these samples may belong to either of these biozones. In general we have *W. Britannica (Fig. 43), W. aff. W. manivitae*, *W. barnesiae, W. Fossacincta,* and *C. margerelii (Fig. 44)* in sample no. TO 75. While *W. britannica, W. manivitae, W. aff. W. manivitae*, *W. barnesiae, Triscutum sp. (Fig. 45), Discorhabdus* sp.*, Biscutum* sp. (*Fig. 46*)*,* and *Schizosphaerella puntulata (Fig. 47)* were detected in sample no. TO 76.

Sample TO 81:

This sample contains *Zeugrhabdotus*, a genus that appears in the middle to upper part of biozone NJT 14. While the primary marker for biozone NJT 14, *Faviconus multicolumnatus*, was not identified, the presence of *Zeugrhabdotus (Fig. 48)* suggests that this sample—and potentially the preceding samples (TO 75 and TO 76)—may also

belong to NJT 14. Biozone NJT 14 is representative of the Kimmeridgian. *Zeugrhabdotus* sp, *W. britannica, W. aff. W. manivitae*, *W. fossacincta,* and *Diazomatolithus Lehmanii (Fig. 49)* were identified in this sample.

Sample TO 83:

W. britannica, W. manivitae, W. aff. W. manivitae, and *W. Fossacincta (Fig. 50)* were noted in the sample.

Sample TO 97:

W. britannica, W. manivitae (Fig. 51), W. aff. W. manivitae, *W. Fossacincta, Discorhabdus* sp. (Fig. 52), and *Schizosphaerella punctulata* were identified in the sample.

In conclusion, the biostratigraphic results indicate a stratigraphic succession spanning from the lower-middle Oxfordian (NJT 13a) through the upper Oxfordian (NJT 13b), potentially into the Kimmeridgian (NJT 14), and uncertainty before sample TO 42 that can be Callovian-Oxfordian because the lack of the nannofossils abundance there (Fig 53; Table 1).

Sample no.	Height (m)	Total abundance	*Biscutacean*	*Cyclagelosphaera sp.*	*C. margerelii*	*Discorhabdus sp.*	*D. lehmanii*	*L. Sigillatus*	*S. puntulata*	*Triscutum sp.*	*Watznaueria sp.*	*W. Barnesiae*	*W. Britannica*	*W. Fossacincta*	*W. aff. W. Manivitae*	*W. Manivitae*	*Zeughrabdothus sp.*	Nannofossils biozones	Age
TO 14	10.05	B	-	-	-	-	-	-	-	-	-	-	-	-	-	-	-	NJT 13a	L-M Oxf.
TO 42	51.35	F	?	-	?	-	-	?	-	-	++	-	+	-	?	?	-		

TO 44	52.25	F	-	?	-	-	-	-	-	-	+	-	++	++	++	-	-	NJT 13b	Upper Oxfordian
TO 52	75.4	B	-	-	-	-	-	-	-	-	-	-	-	-	-	-	-		
TO 55	80.9	R	-	-	-	-	-	-	-	-	-	-	+	-	++	-	-		
TO 59	85.45	R	-	-	-	-	-	?	-	-	+,?	+	+	-	+	+	-	Uncertain	Uncertain
TO 69	93.8	B	-	-	-	-	-	-	-	-	-	-	-	-	-	-	-		
TO 72.	96.25	B	-	-	-	-	-	-	-	-	-	-	-	-	-	-	-		
TO 75	100.5	F	-	-	+	-	-	-	-	-	+	+	+	+	+	-	-		
TO 76	101.2	C	+,?	-	-	+,?	-	-	+	?	+	+	+,?	-	++	++	-	NJT 14	Kimmeridgian
TO 81	102.75	F	-	-	-	-	?	-	-	-	+	-	++	++	++	+	+		
TO 83	103.5	C	-	-	-	-	-	-	-	-	+	-	+	+	+	+	-		
TO 94	109.35	B	-	-	-	-	-	-	-	-	-	-	-	-	-	-	-		
TO 97	111.6	C	-	-	-	+	-	-	+	-	+	-	+	+	+	+	-		

Table 1. Calcareous nannofossil species distribution in the log plotted against age.

Notes to Table 1: Calcareous nannofossil species abundance was semiquantitatively estimated Total abundance. C = common: equal or more than 20 were detected; F = few: equal to 15 or more; R = rare: Less than 15 samples were detected; B = barren. Species abundance. (+) present; (++) present with high amount; (-) free; (?) maybe/ comper to "cfr".

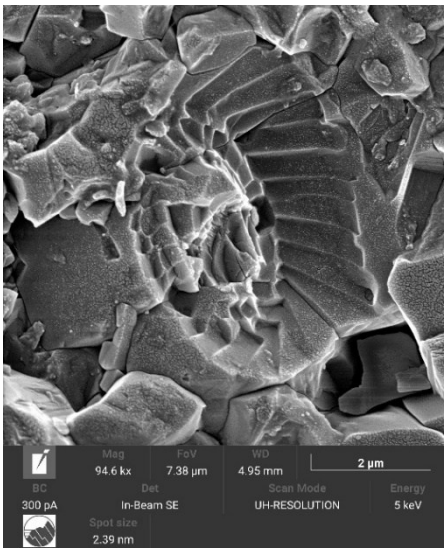

Fig 38. *L. Sigillatus (TO42)*

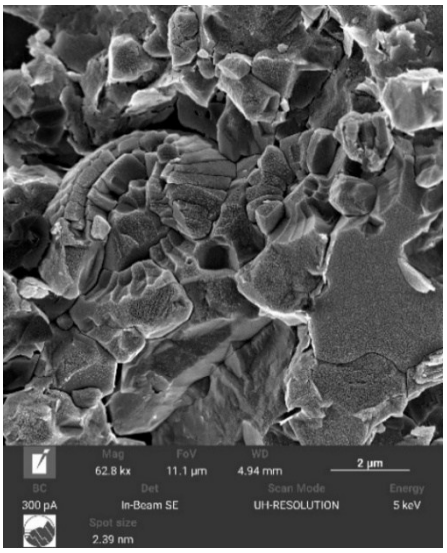

Fig 39. *C. margerelii (TO42)*

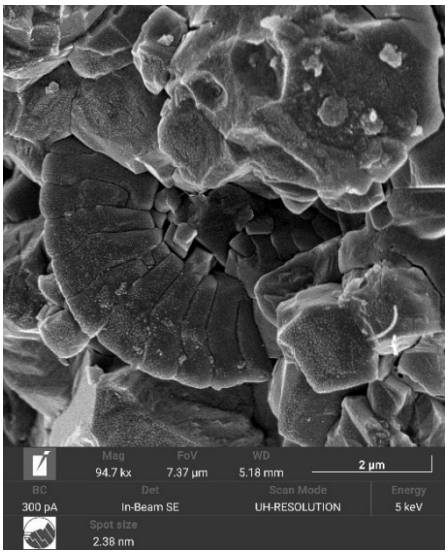

Fig 40. W. aff. W. manivitae (TO44)

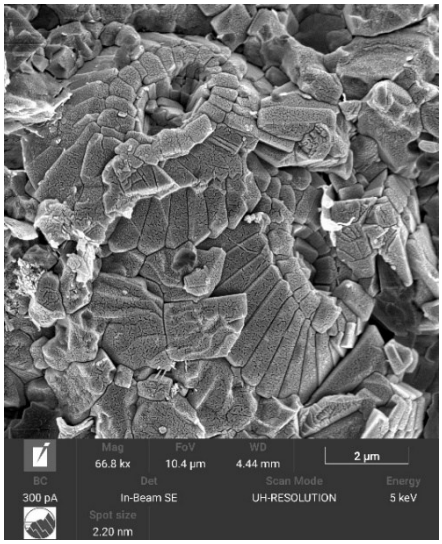

Fig 41. W. britannica (TO55)

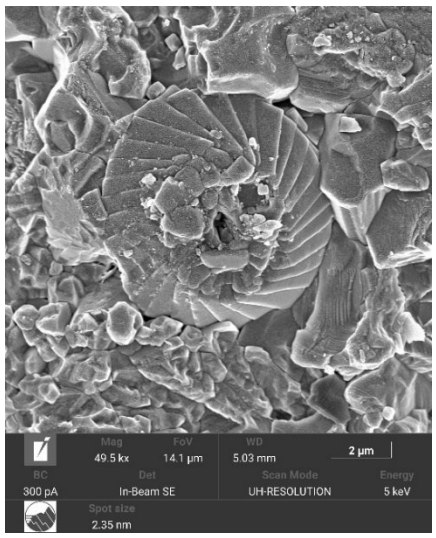

Fig 42. W. barnesiae (TO59)

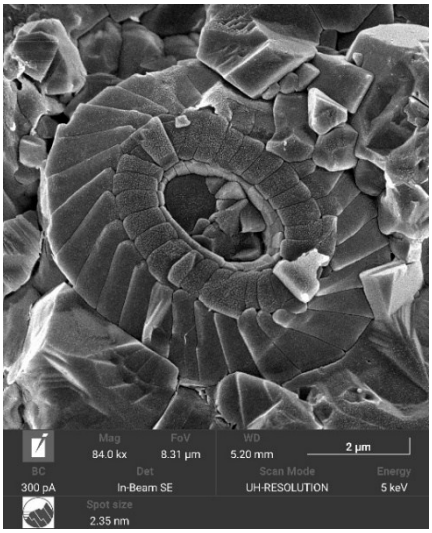

Fig 43. W. britannica (TO75)

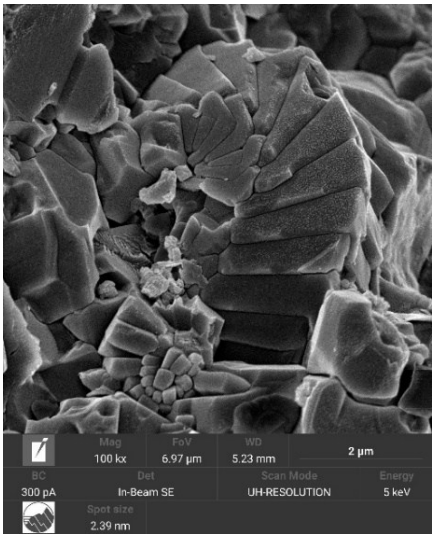

Fig 44. C. margerelii (TO75)

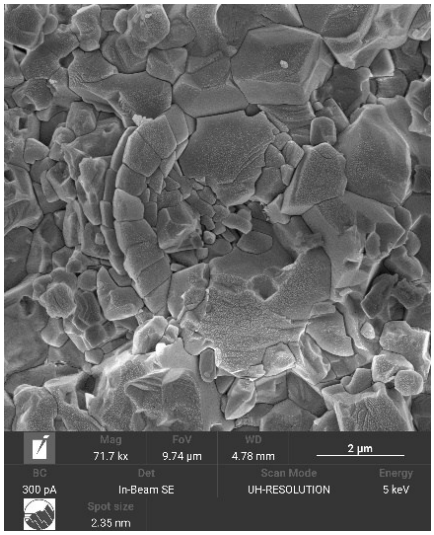

Fig 45. Triscutum sp. (TO76)

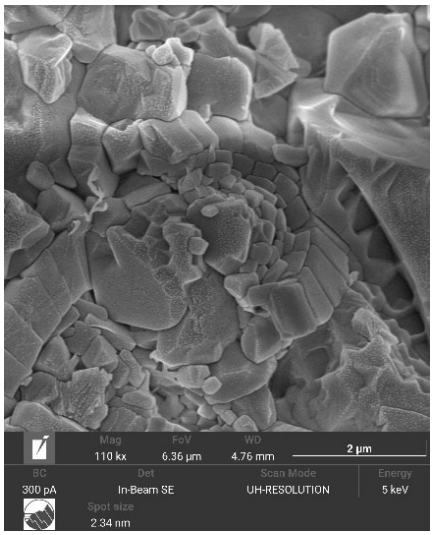

Fig 46. Biscutum sp. (TO76)

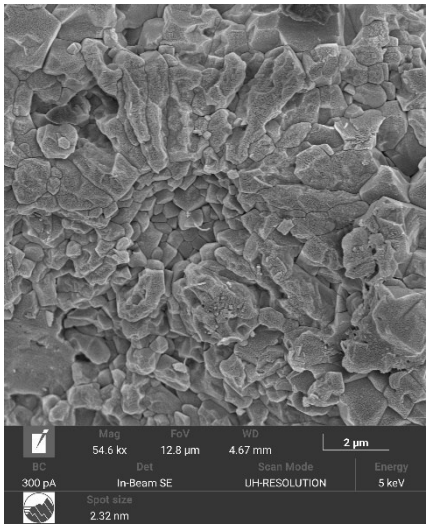

Fig 47. S. puntulata (TO76)

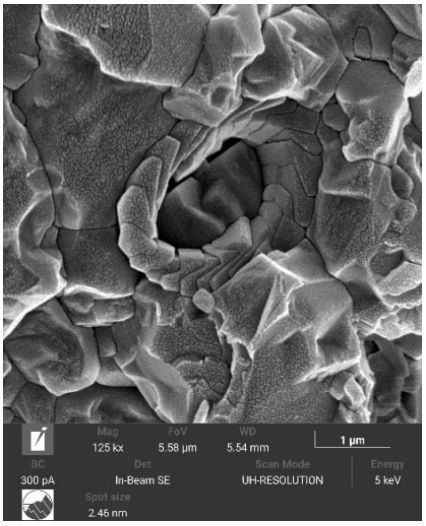

Fig 48. Zeugrhabdotus sp (TO81)

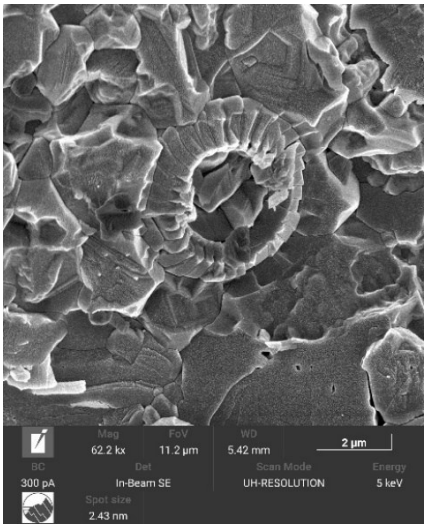

Fig 49. D. Lehmanii (TO81)

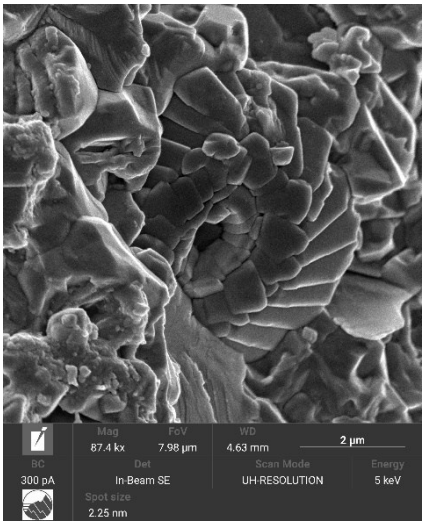

Fig 50. W. fossacincta (TO83)

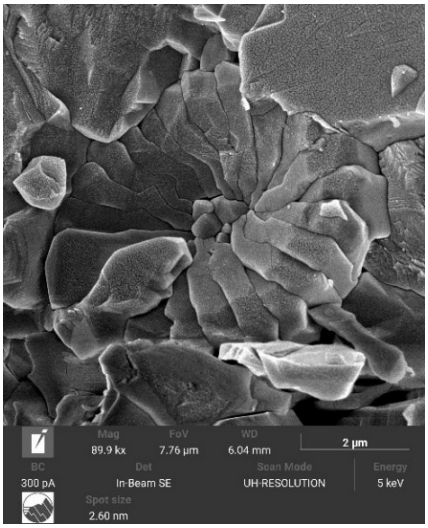

Fig 51. Discorhabdus sp. (TO97)

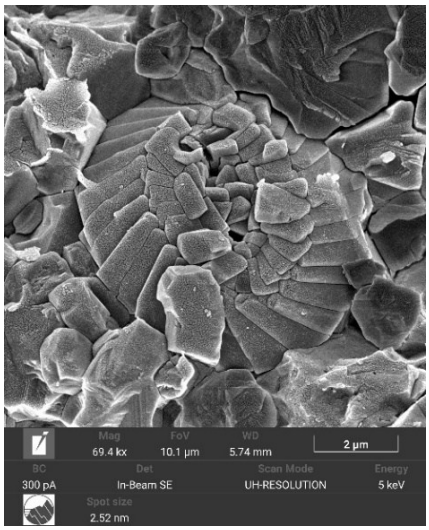

Fig 52. W. Manivitae (TO97)

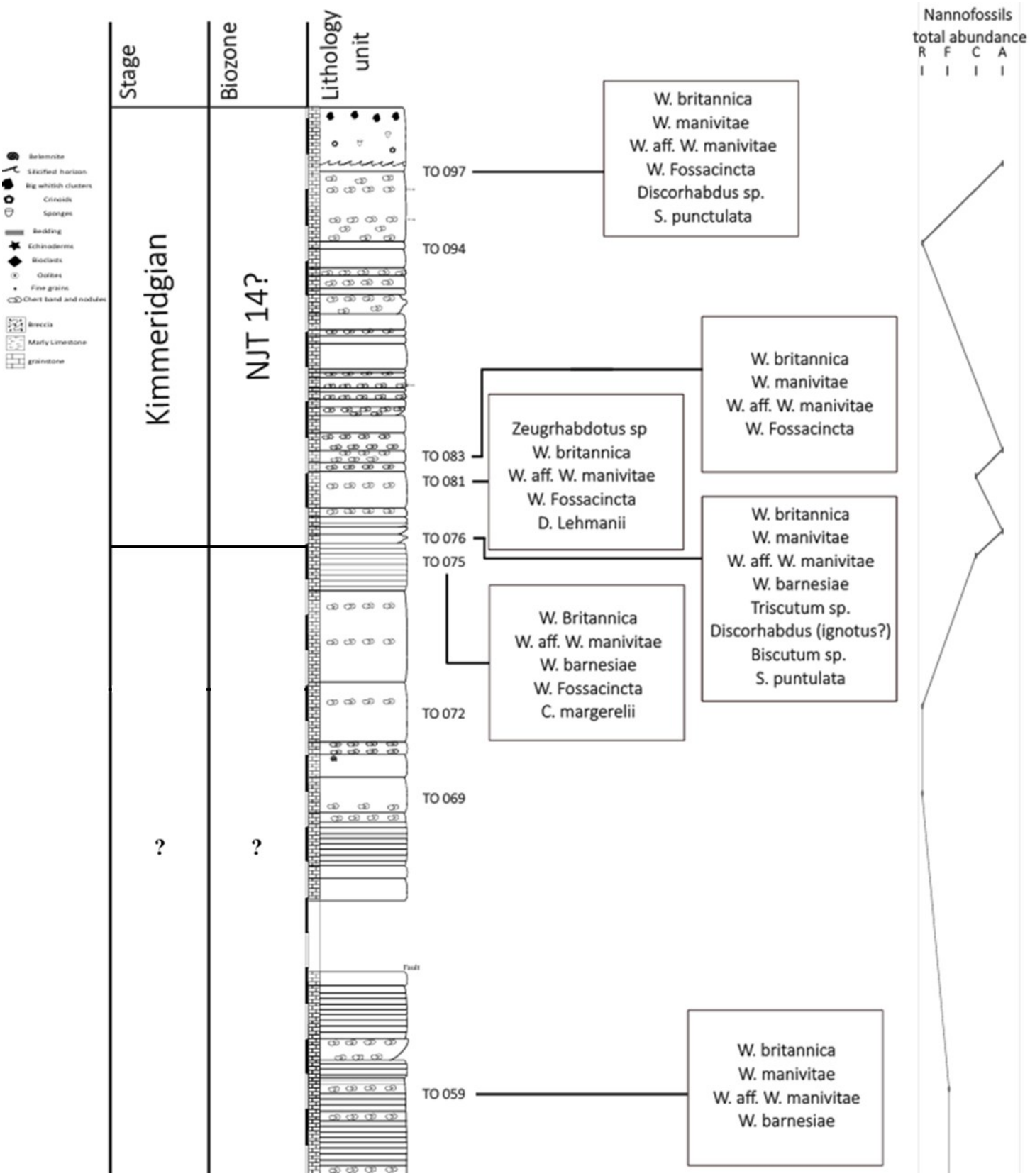

Figure. 53. The Stratigraphic columns of the section with sample numbers alongside biostratigraphic data, the question mark represents an uncertain period.

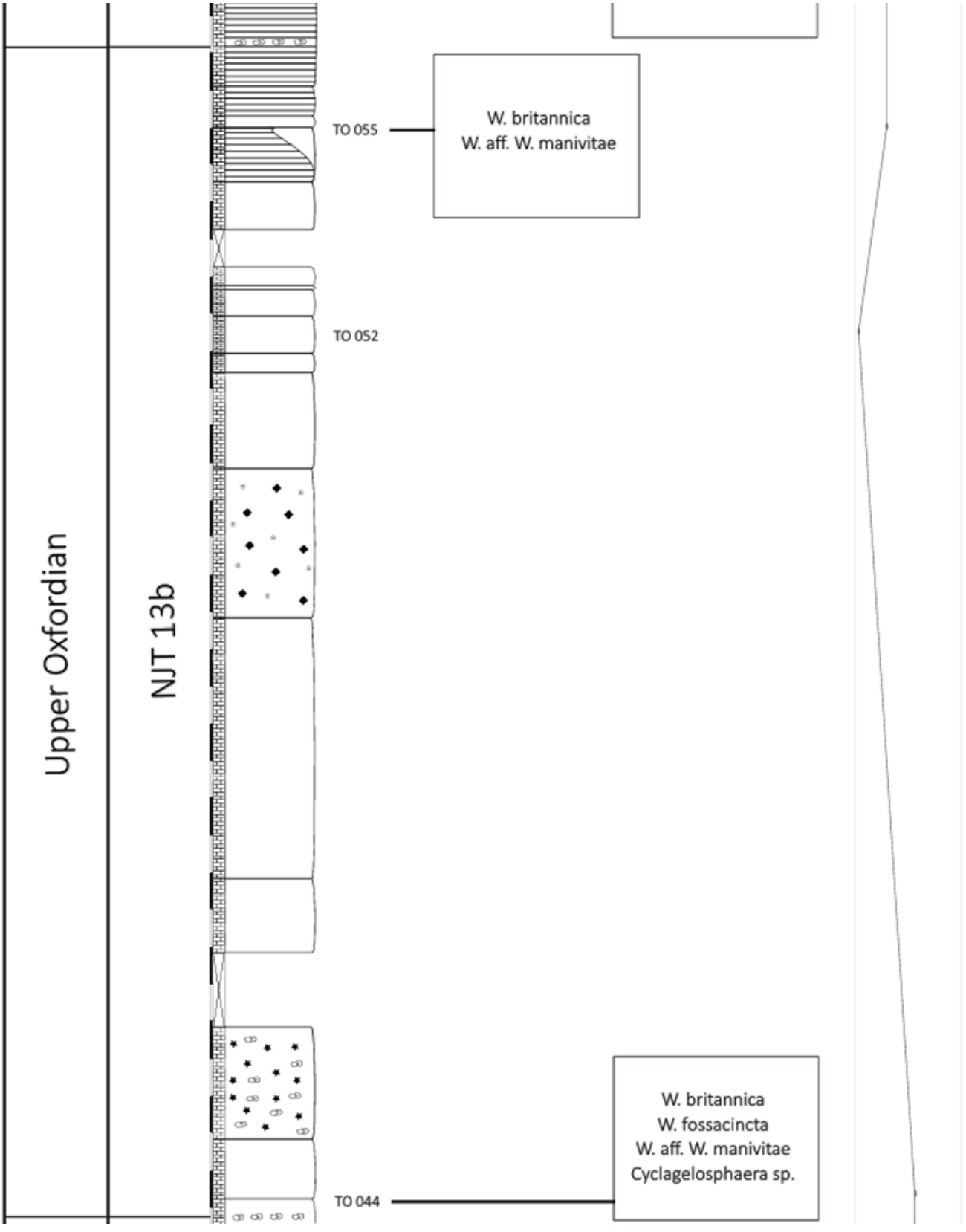

Figure 53. (*continued*).

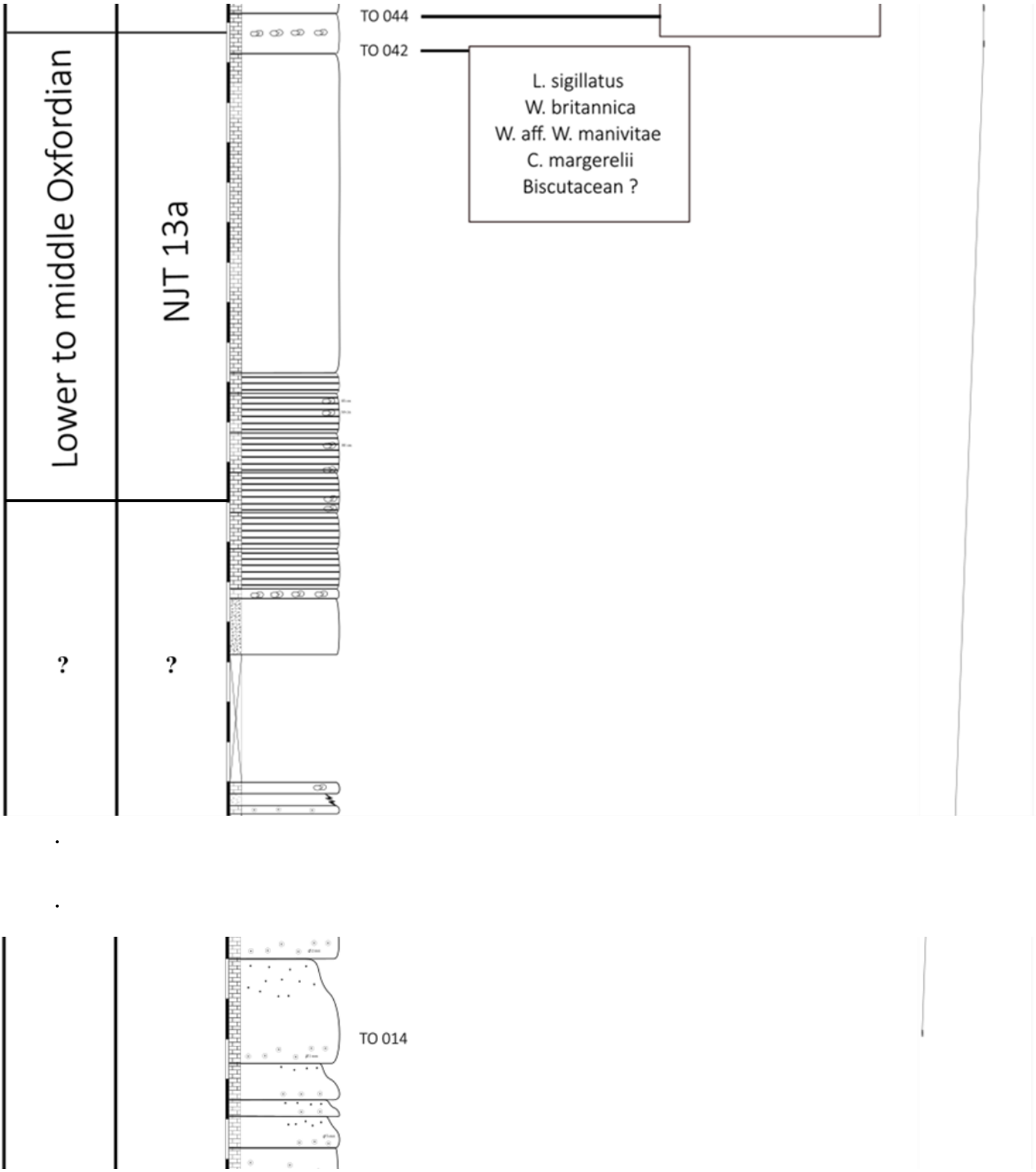

Figure 53. (*continued*).

3.4. Quantitative petrography for ooids

A preliminary examination of the samples revealed distinct variations in the ooids' size, type, mineralogy, abundance, and preservation, allowing them to be classified into different categories.

3. 4. 1. Ooid Size and Distribution

The analyzed dataset displays a wide range of ooid sizes, from 73 µm to 1641.5 µm, with the average 50th to 75th percentiles being at 270 and 370 µm. It also shows a visibly increasing trend in the ooid mean size with some swings throughout the whole section.

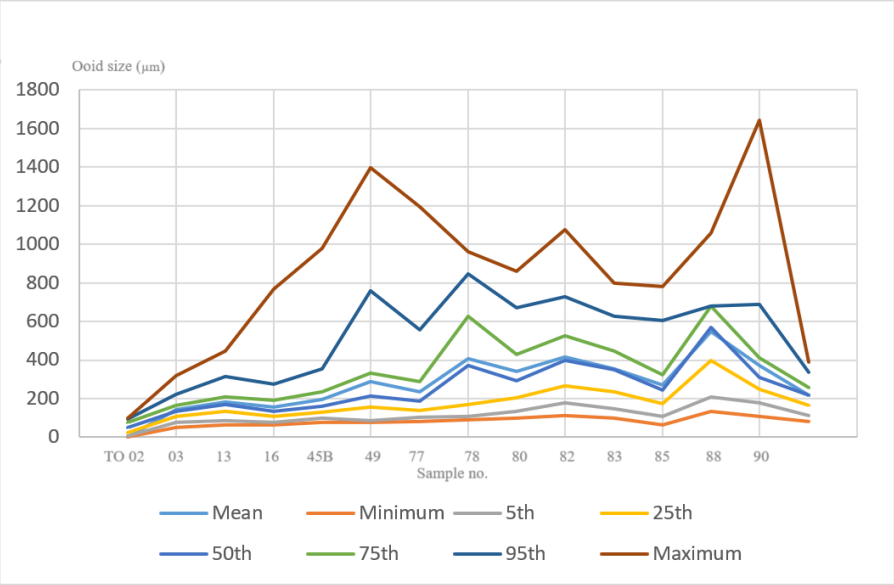

Figure 54. Cross plot for different measurements of the ooids.

Oxfordian Trends:

The mean ooid diameter remains relatively stable in the Oxfordian, particularly in the lower to middle Oxfordian, fluctuating between 146 and 301 µm, with an average of 205 µm. A more noticeable increase occurs in the upper Oxfordian, where a small number of exceptionally large ooids (>1000 µm) are recorded (Fig. 54 & 55; Table 2).

The overall mean size across the Oxfordian samples is 205 µm, with the 50th, 75th, and 100th percentiles at 170 µm, 244 µm, and 850 µm, respectively, with a general growing trend with two small crests in sample TO 03 and TO 45B.

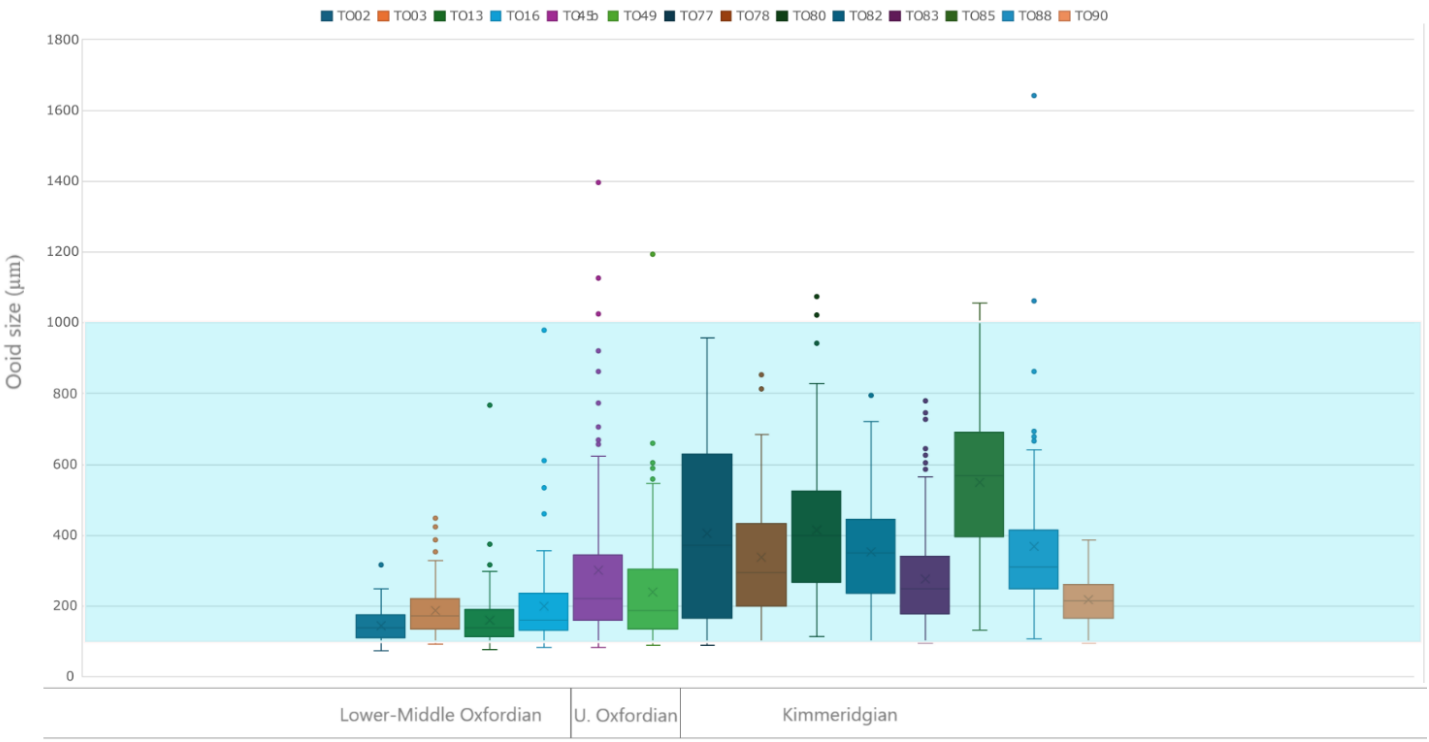

Figure 55. The size distribution of the ooid long-axis measurements (µm). The light blue area represents the recorded size of Upper Jurassic ooids globally, according to Koeshidayatullah et al. (2022). The measurements of Koeshidayatullah et al., (2022) on the graph refer to the minimum size to the 95th percentile; the maximum value reached was 3000 µm, which wasn't recorded directly inside the study but was reported.

Kimmeridgian Trends:

In contrast to the Oxfordian, the Kimmeridgian exhibits a broader range of ooid mean diameters between 218 to 549 µm, with an average of 365.5 µm, accompanied by more pronounced fluctuations. Notable peaks occur in the following samples:

The 50th, 75th, and 100th percentiles reach 372, 629, and 959 µm in sample TO 77, reach 400, 524, and 1073 µm in sample TO 80, and 568, 681, and 1057 µm in sample TO 85.

Across the entire section, the overall diameters for the Kimmeridgian samples are 345 µm (50th percentile), 464 µm (75th percentile), and 945 µm (100th percentile). Here we have large ooids (between >1000 µm and <2000 µm) in three samples but still, no giant

ooids (>2000 μm) were recorded. Examining the Oxfordian–Kimmeridgian interval as a whole, most recorded ooids fall within the ≤1000 μm range, with large ooids (>1000 μm but <2000 μm) occurring in only five samples out of fourteen, and no giant ooids (>2000 μm) recorded, and with a mean average equal to 297 μm (Fig. 54 & 55; Table 2).

Sample no.	Age	Height (m)	Mean (μm)	Percentile						
				Min	5th	25th	50th	75th	95th	Max
TO 02	Lower-Middle Oxfordian	1.7	145.7	73	88.3	111.1	139.7	174.6	222.9	317.5
TO 03		2.3	187	92.1	105.7	136.5	171.5	220.7	319.9	447.7
TO 13		9.65	158.9	76.2	85.7	114.3	139.7	190.5	276.9	768.4
TO 16		12.1	199.1	82.6	101.4	132.6	158.8	235.7	352.6	977.9
TO45B	U. Oxfordian	53.9	300.6	82.6	104.6	161.1	220.7	343.7	779.1	1397
TO 49		70.6	238.9	88.9	108	139.7	187.3	298.5	558.8	1193.8
TO 77	Kimmeridgian	101.4	406	88.9	107.8	169.9	371.5	628.7	845.7	958.9
TO 78		101.55	339.4	98.4	133.8	202.4	293.7	427.8	672.1	860.4
TO 80		101.85	413.7	114.3	180.3	266.7	400.1	523.9	726.4	1073.2
TO 82		103.25	352.3	98.4	148.4	237.3	350.8	444.5	628.7	796.9
TO 83		103.5	276.1	95.3	116.9	177.8	247.7	336.6	610.2	781.1
TO 85		104.4	548.7	133.4	208.9	396.9	568.3	681	681	1057.3
TO 88		106.35	369.5	108	178	249.2	311.2	412.8	688.8	1641.5
TO 90		106.95	217.9	95.3	114.3	165.1	215.9	258.8	336.6	387.4

Table 2. Ooid size distribution across the Oxfordian-Kimmeridgian.

3. 4. 2. Ooid Textures and Microstructure

Petrographic analysis here was narrowed for only the ooids that were used in the size measurements, it revealed two dominant ooid types: micritic and radial ooids which were detected throughout the whole section but with different ratios. The proportion of micritic ooids is 45 to 60 percent and remains nearly constant with only a slight increase in the lower-middle Oxfordian especially sample TO 02,13,16 (Fig. 56). Then the ratio of the Micritic vs. Radial ooids increases notably in the upper Oxfordian.

During the Kimmeridgian, there is a clear trend with increasing the radial ooids. Samples TO 77,78,80,82 which have a generally high ratio of the radial vs. micritic ooids (Fig. 57), then it keeps increasing and becomes dominant from sample TO 83 till it will be nearly a pure thin section of radial ooids in sample TO 90 (Fig. 58).

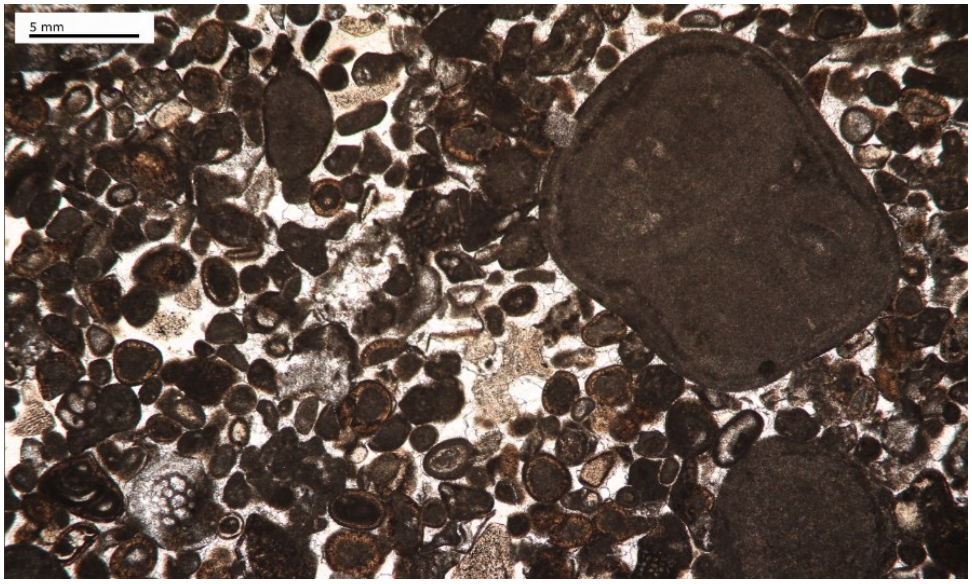

Figure 56. Grainstone with micritic and radial ooids with a big intraclast in the upper right corner, sample 16, the photo was taken by a digital camera for the microscope.

This indicates a shift in the depositional conditions but also an insight into mineralogy, where low-magnesium calcite (LMC) ooids typically show radial fabrics. In the case of the micritic ooids, it occurred due to the micritization process as a result of microbial activity and diagenetic alteration, which can overprint the primary structures, making it hard to determine the original mineralogy. It was also noted a complete absence of tangential or replaced ooids throughout the whole section, which would be typical in the

case of aragonite or, in some cases, high-magnesium calcite (HMC) ooids (Rankey & Reeder 2000).

Ooids have different degrees of alteration, which will be discussed in the following chapter.

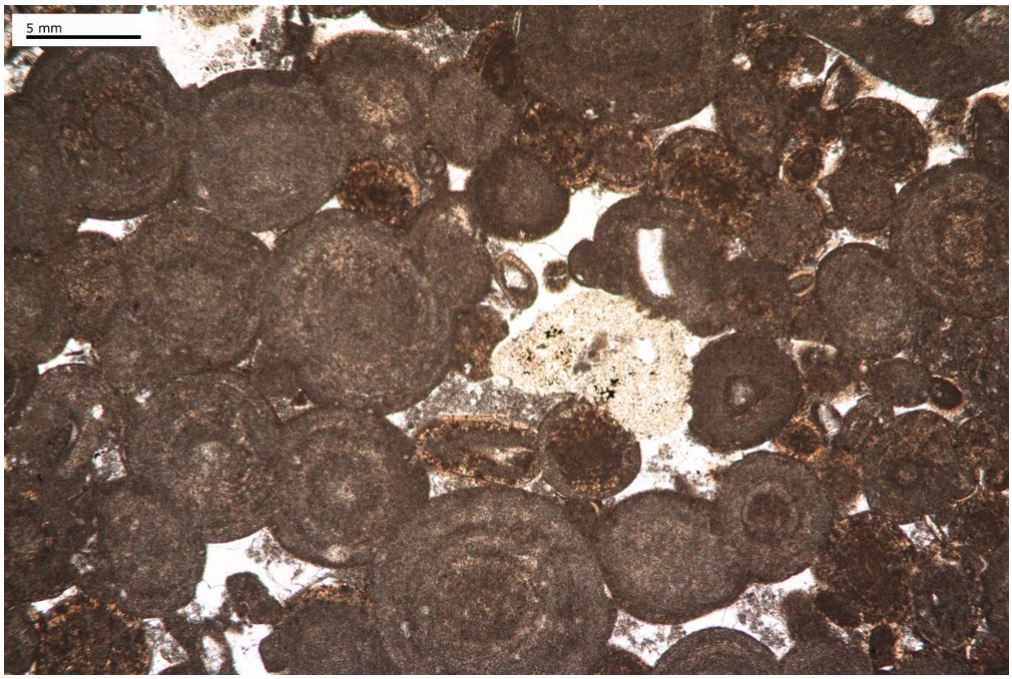

Figure 57. Grainstone with a high amount of radial ooids vs. micritic ones, sample 80 (PPL), the photo was taken by a digital camera for the microscope.

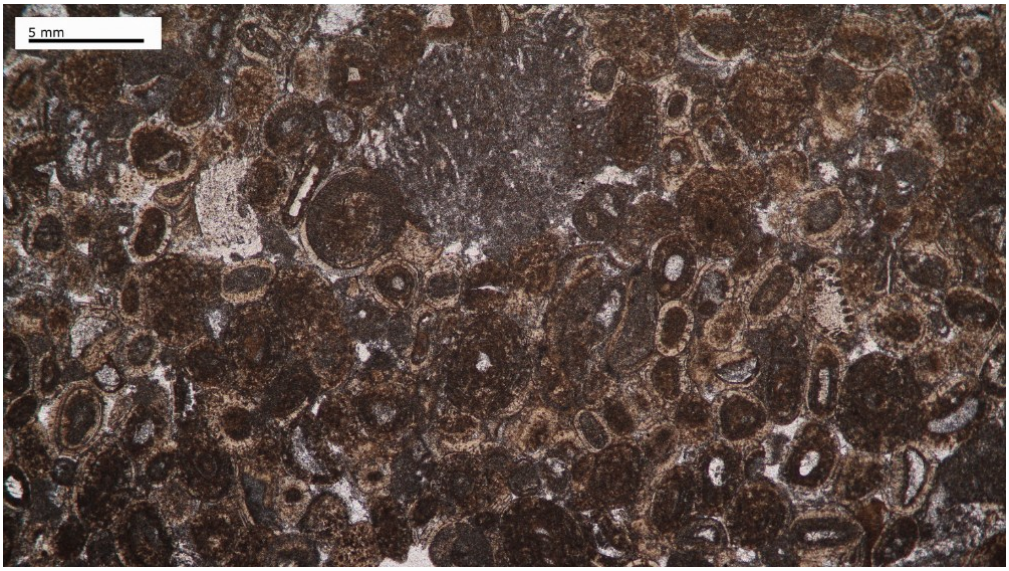

Figure 58. Grainstone with radial ooids, sample TO 90 (PPL), the photo was taken by a digital camera for the microscope.

3. 4. 3. Ooid Abundance and Stratigraphic Trends

The abundance of ooids in calciturbidites through the section changes dramatically. In the lower to middle Oxfordian ooids are abundant but decrease in the upper Oxfordian. In the upper part, some calciturbidites were so poor in ooids that qualification could not be performed. Then, the Kimmeridgian ooids return with great abundance and increase in size. The abundance decreases again in the last part of the section.

In conclusion, the main ooid features divided the samples into different sections: samples TO 2, 3, 13, and 16 share more or less the same size and degree of abundance, next to a greater presence of micritic ooids - albeit radial ooids are the most abundant. These samples represent the early to middle Oxfordian.

Then samples TO 45B and 49 here are similar in the size, abundance, and proportion of micritic ooids. These samples are dated to the late Oxfordian.

For the Kimmeridgian samples, the ooid size has an increasing trend from TO 77 to 85 just with one notable exception in sample TO 90. The abundance of the radial ooids over micritic ooids is higher than in the Oxfordian.

4. Discussion

4. 1. The stratigraphic results

Overall, the stratigraphic log captures two out of three distinct members of the Fonzaso formation: the lower oolitic member (Upper Bathonian to the Lower Oxfordian) and the skeletal member (Middle Oxfordian to the Kimmeridgian), with a possibly younger age for the intermediate "skeletal" member leading to the final nodular member of the Fonzaso formation, for the presence of the last section 2m that can represent a possible transition section from the skeletal to the nodular member. which means, our section can be identified between the Upper Bathonian to Kimmeridgian, if the two members were observed completely in the fieldwork.

4. 2. Stable isotopic correlation with the Adriatic Platform

Moving forward to the isotopic results, and comparing them with previous literature, especially as reported by Husinec et al. (2022), we had quite good correspondence with the isotopic values of The Adriatic Carbonate Platform, Croatia where $\delta^{13}C$ values generally range from -1.8 to +4‰ (mean +1.9‰), and $\delta^{18}O$ from -3.5 to +3.1‰VPDB (mean 1.1‰), and our section ranges from -0.81 to +4.03 ‰ (mean +2.51‰) for the $\delta^{13}C$ values, and $\delta^{18}O$ from -4.45 to -0.14 ‰VPDB (mean -2.29‰).

4. 2. 1. Oxfordian age

We can see similarities between the first section of our log which represents the first 90 meters there and the DJ section, with nearly all the important anomalies and their values. For instance, in our records, just before the transition to Kimmeridgian, $\delta^{13}C$ increase in our section, followed by a decrease near the boundary, to reach the lowest value at sample TO 66, which is aligned perfectly with the case of the DJ section (Fig. 27 & 28). The Oxfordian is represented here by the first 90 m in the log.

4. 2. 2. Kimmeridgian age

From sample TO 67 to the end of the log covers the last 20 meters. The BG-BK section of the Dinaric platform shows similar trends and values as was mentioned in the results chapter, particularly for the first part of the BG section (Fig. 31 & 32), with a negative excursion to -0.81‰ at 97.65 m. After that, a positive trend follows that peaks at meter 107.55 m with a $\delta^{13}C$ value of 4.03 ‰. Based on the isotopic correlation with the Dinaric platform, the Kimmeridgian in our section is incomplete, as we did not reach the Kimmeridgian/Tithonian boundary.

4. 3. The global correlation

The $\delta^{13}C$ values for the two ages in our section are generally similar to the values from coeval Ammonites and belemnites (+1 to +3‰), also brachiopods and oysters although they usually show a wider range (+1 to +4‰) (Dera et al., 2011) suggesting that they have not been significantly reset by diagenesis.

The $\delta^{13}C$ (Fig. 24) is characterized by high frequency but low-amplitude (generally less than 2‰) variability. This is consistent with the absence of hyperthermal events during the Late Jurassic, not just around the platform but more or less globally (Jenkyns et al., 2002). However, moderate amplitude $\delta^{13}C$ oscillations reflect less extreme climate instability.

4. 4. Refining the age by the SEM

The results of biostratigraphy may be imperfect because of the low number of individuals we found with respect to a smear slide preparation. However, we could not do smear slides because all facies in the section are well-cemented limestones.

We couldn't represent the first part of our log before sample TO 42 with any fossils due to the small abundance of the nannofossils which is a common condition in this period anyway. So the results show uncertainty in the first part of the log before this sample which can be put to Callovian - Oxfordiam, and uncertainty extends to also the boundary between the Oxfordian and Kimmeridgian, precisely from sample TO 59 to TO 72 because of the insufficient recovery of nannofossil markers.
In general, the results confirmed the stable isotope results in identifying the two ages: Oxfordian (with even more details in its internal sections) lower-middle Oxfordian (NJT 13a) represents sample TO 42, then the upper Oxfordian (NJT 13b) represents sample (TO 44 to TO 55), and then potentially into the Kimmeridgian (NJT 14) from the sample (TO 75 to TO 97) (Fig. 53).

4. 5. Ooid statistical measurements in the Belluno Basin

4. 5. 1. Ooid size and its abundance

The dataset reveals ooid sizes ranging from 73 μm to 1641.5 μm, with a generally increasing trend, albeit with fluctuations. While Oxfordian mean size remains relatively stable with an average of 205 μm, a slight increase occurs in the upper Oxfordian, where exceptionally large ooids (>1000 μm) also appear. The Kimmeridgian ooids have a wider size range, with an average of 365.5 μm and more pronounced fluctuations, large ooids were detected there too.

Apparently, we recorded abundant ooids later than Picotti and Cobianchi (2017), i.e., well into the Kimmeridgian, therefore extending the range of ooid production on the nearby Friuli platform with respect to what was thought so far. Biostratigraphic determination awaits confirmation by further analyses on smear slides, either here or from correlated sections.

Ooids' abundance in the calciturbidites varies significantly throughout the section. In the lower to middle Oxfordian, ooids are abundant but decrease in the upper Oxfordian, where some layers are almost devoid of them. The Kimmeridgian sees a resurgence of

ooids, with an increase in both abundance and size before declining again in the uppermost part of the section.

4. 5. 2. Correlation with global and local Jurassic data

The mean ooid diameters in our section are consistent with the late Jurassic global range values. In comparison, Koeshidayatullah et al., (2022), documented that the interval within the 50th to 75th percentiles of Upper Jurassic ooid size is 470–690 µm (Fig. 55). Also, large ooids were recorded there, and giant ones too but sporadically.

Additionally, the size distribution in our samples closely aligns with that of the Trento Platform during the Early Jurassic, with slightly larger measurements, which follows the established Jurassic trend (Fig. 59; Vulpius & Kiessling, 2017).

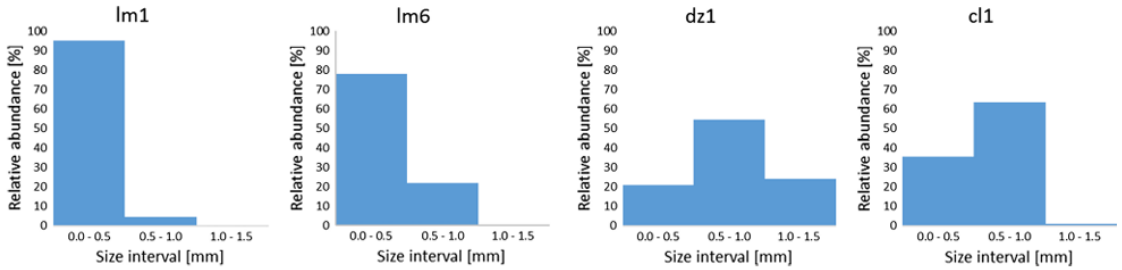

Figure 59. Histograms of ooid size from the sample lm1 from the Hettangian, lm6 from the Sinemurian, dz1 from the Pliensbachian, and cl1 from the Toarcian. All kinds of ooids were counted even the micritized ooids (Vulpius & Kiessling, 2017).

4. 6. The mineralogy of the ooids

4. 6. 1. Preservation degree and Mineralogical Composition

According to Vulpius and Kiessling (2017), the general category of preservation is related to the original mineralogy of the ooid and can be:

Well-preserved ooids – Clearly visible nucleus, that is distinguished from the rest of the ooid layers, well-defined concentric layers, and intact radial or tangential crystal structures. These ooids were likely low-magnesium calcite (LMC) or high-Mg calcite (HMC), as there is no evidence of dissolution or recrystallization which is instead affecting aragonite fossils (e.g., corals) in the same samples.

Moderately preserved ooids – Nucleus still discernible but partially micritized, with radial/tangential structures appearing faint. The presence of micrite and microspar suggests partial recrystallization from HMC, or aragonite, to LMC.

Micritized ooids (poor preservation) – The nucleus is not separated unless it is recrystallized and appears as a homogeneous black micritic texture with an exception for some microspar and with little to no visible structure. The original mineralogy is unclear, but the complete micritization suggests extensive diagenetic alteration.

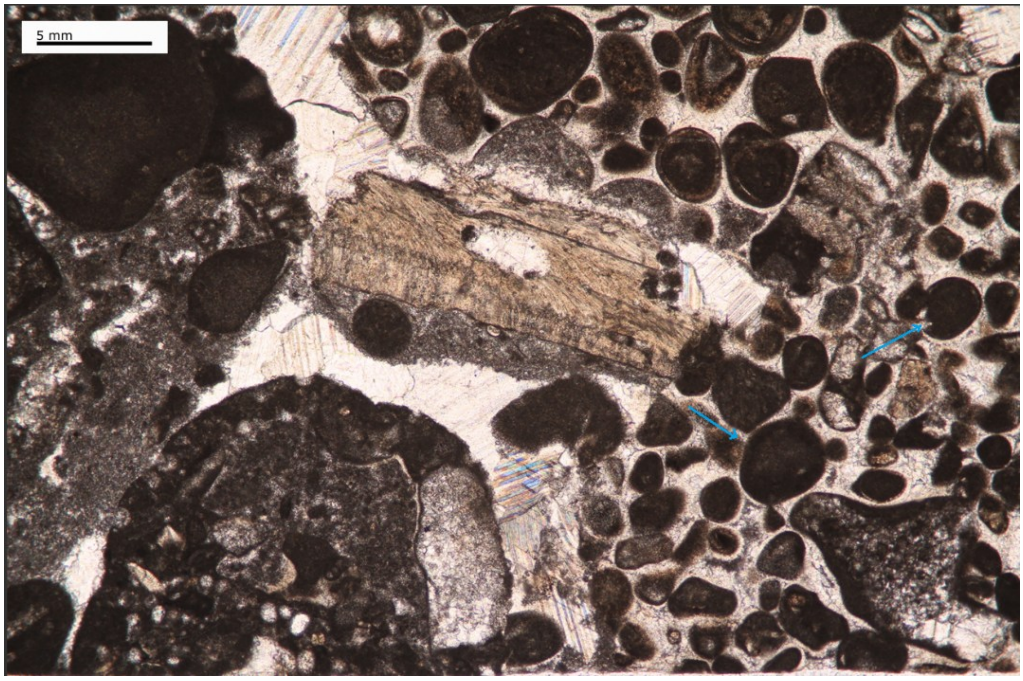

Figure 60. Sample TO 45 (PPL), the blue arrows point to some of the micritized ooids, the photo was taken by a digital camera for the microscope.

In our studied samples, the preservation states vary significantly across the section. More micritized ooids and moderately preserved ooids were observed than well-preserved ooids which were expected in the case of a calcite sea. Most of the samples have some micritized ooids. The number of micritized ooids is rather high, especially at the beginning of the section, like in the case of samples TO 02, 16, and 45B (Fig 60), with a

fair increase in the number of moderately preserved ooids in samples TO 03 and 13. Above, the moderately preserved ooids increase dramatically in samples TO 77, 78, 80, and 82 (fig. 61) and even more in samples TO 83, 85, 88, and 90. Also, well-preserved ooids increase in abundance (Fig. 62).

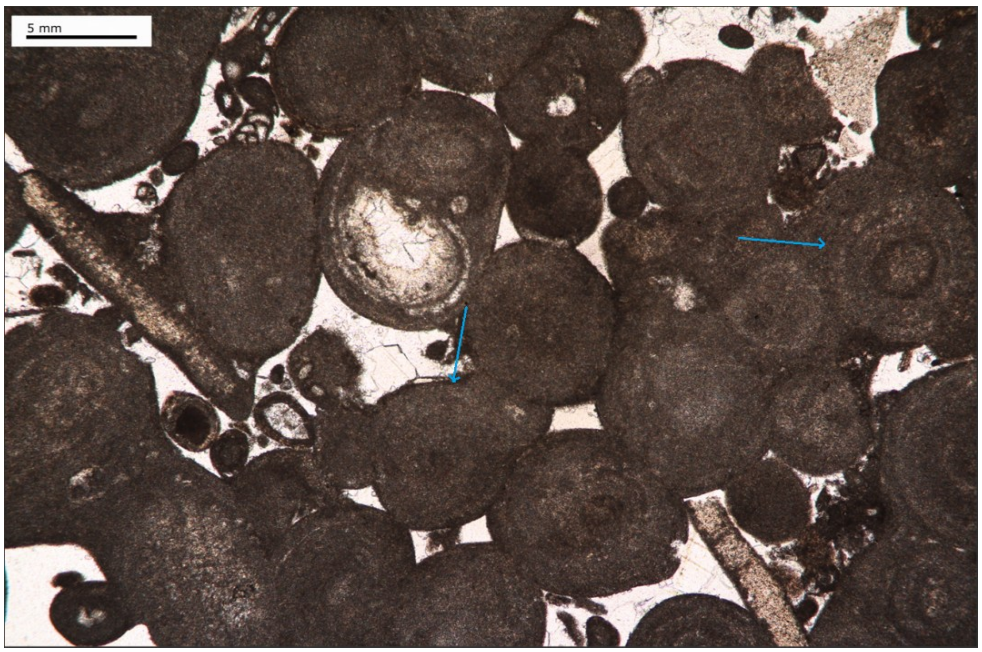

Figure 61. Sample TO 77 (PPL), the blue arrows point to some of the moderately preserved ooids, the photo was taken by a digital camera for the microscope.

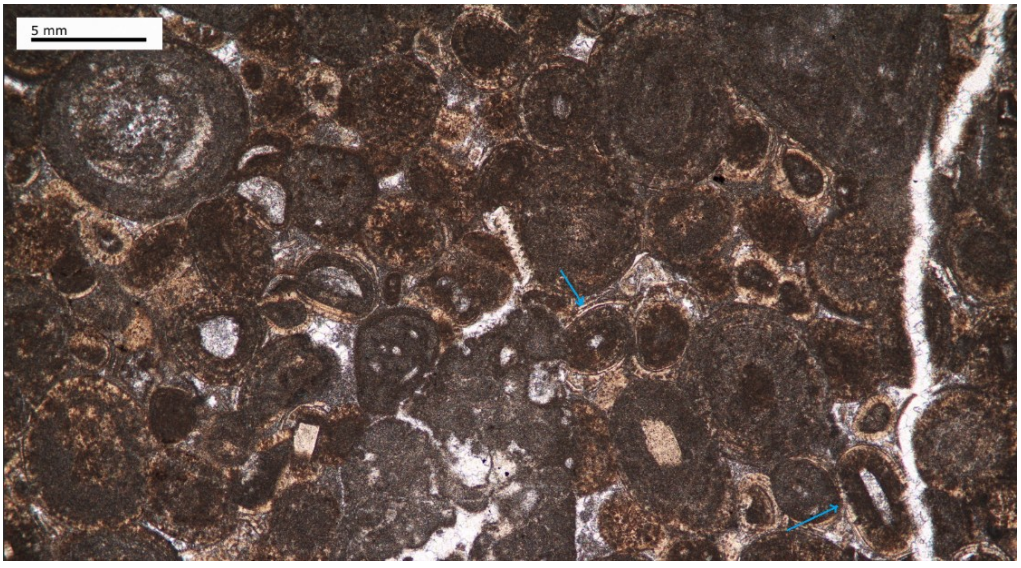

Figure 62. Sample TO 88 (PPL), the blue arrows point to some of the well-preserved ooids, the photo was taken by a digital camera for the microscope.

The preservation doesn't have a specific trend in our samples, except for a gradual increase in preservation upward, so overall, it's better during Kimmeridgian compared to the Oxfordian, which may reflect an increasing proportion of LMC ooids versus HMC ooids, according to Vulpis and Kissling 2017.

However, we did not observe any spatial differentiation between the three types of preservation. Micritic, micritized radial and well-preserved radial ooids are found together in the same sample, often in the same field of view. For instance, in samples TO 80, 82, and 83 (Fig 63), we have very well-preserved ooids, next to badly preserved ones. Although this has been reported in some samples of Vulpius and Kissling 2017, in our samples it occurs systematically. So we conclude that alteration is a criterion too weak to be trusted here for the distinction between ooids with HMC and LMC mineralogy.

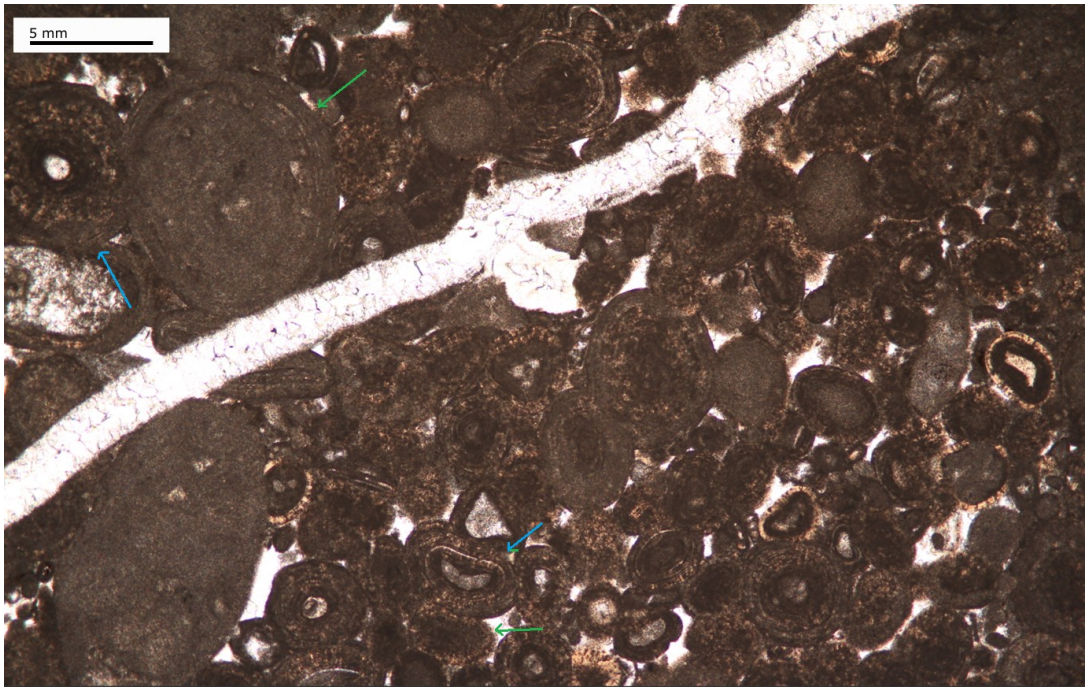

Figure 63. Illustrate the different degrees of preservation at the same FOV - The blue arrows point to the well-preserved ooids, while the green ones show the micritized radial, sample TO 82 (PPL), the photo was taken by a digital camera for the microscope.

4. 6. 2. Ooid Textures and Mineralogical Composition

According to texture petrographic analysis, micritic and radial ooids were identified as the dominant types, with varying ratios throughout the section. Micritic ooids remain

relatively constant but slightly increase in the lower-middle Oxfordian, then become more dominant in the upper Oxfordian. Radial ooids increase significantly during the Kimmeridgian, becoming dominant from sample TO 83 onward, with sample TO 90 containing almost exclusively radial ooids. While it is difficult to ascertain the initial mineralogy in the case of the micritic ooids. However, radial fabrics are commonly observed in low-magnesium calcite (LMC) ooids.

Tangential or replaced ooids are completely absent, indicating a lack of any trace of aragonite or high-magnesium calcite (HMC) ooids remaining from the aragonite sea (Rankey & Reeder 2000).

So, all ooids are calcite, with a lack of any evidence for aragonite ooids. There is a degree of uncertainty related to micritic ooids, but it should be noted that aragonite is most commonly replaced by mosaic sparry calcite, rather than by uniform micrite. The observation is in agreement with the calcite-dominated mineralogy expected for the Late Jurassic.

4. 7. The relationship between the ooid size and the chemical and physical properties of the sea

According to (Trower et al., 2022) ooid diameters reflect a dynamic equilibrium between physical abrasion rates and $CaCO_3$ precipitation rates, which are influenced by factors such as carbonate saturation state (Ω) and temperature. Their findings suggest that variations in seawater chemistry can impact ooid size. When Ω is high (seawater is more supersaturated to $CaCO_3$), carbonate precipitation is enhanced, including ooid formation.

Higher $\delta^{13}C$ values often indicate increased carbonate productivity and if carbonate production was high, conditions may have favoured the growth of larger ooids, potentially leading to a positive correlation between ooid size and $\delta^{13}C$ values (Trower et al., 2022).

So by studying the ooid size measurements, the $\delta^{13}C$, and the paleotemperature (Brigaud et al., 2008) parallel to each other during the whole section, we can see sort of a relationship between them, showing nearly a linear relationship between increasing the temperature and the $\delta^{13}C$ accompanied by increasing in the ooid size (Fig. 64).

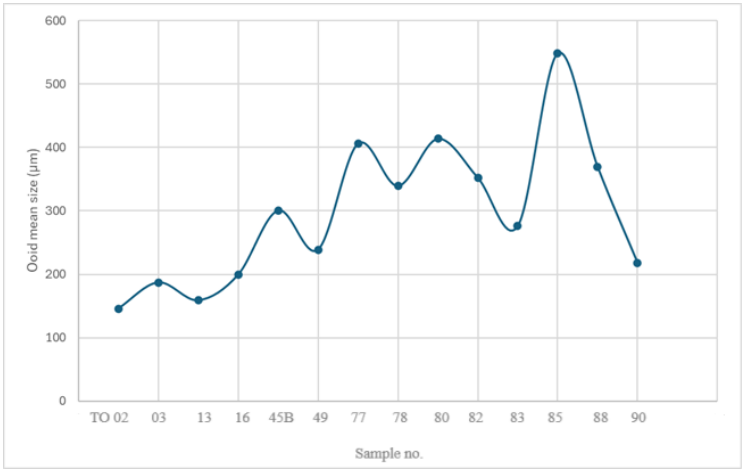

(a)

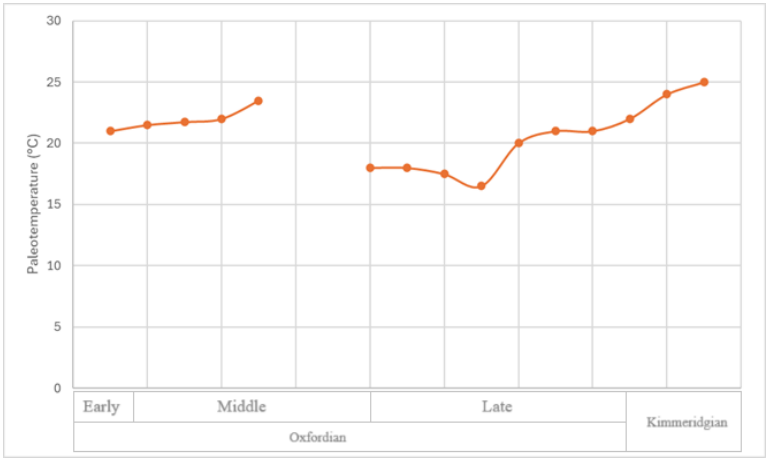

(b)

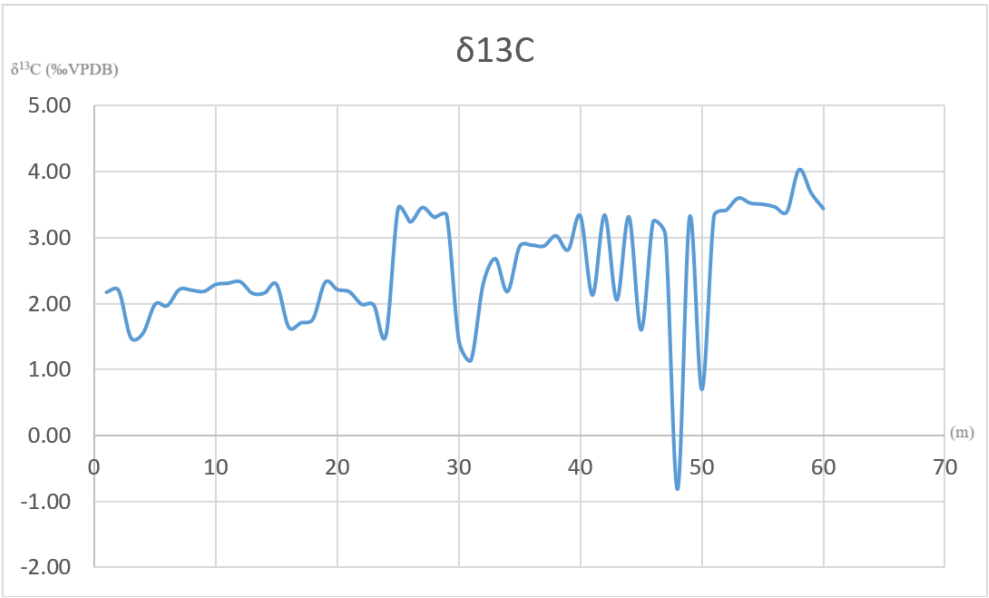

(c)

Figure 64. Illustrates (a) the size distribution of the ooid size measurements (µm), (b) the $\delta^{13}C$ (VPDB) through the whole section, and, (c) the paleotemperature data from (North West Tethyan domain) after (Brigaud et al., 2008) - for the Jurassic period, previous studies (Picard et al., 1998) have proposed a temperature decrease of 3.5 °C in the first 50 m of the water column based on δ18O values of fish tooth apatite and brachiopod calcite. While Ooids typically form and accumulate in water depths < 5 m (up to 10-15 m).

5. Conclusion and future work

The size distribution, preservation, and mineralogical composition of Middle-to-Late Jurassic ooids in the Belluno Basin's calciturbidites are examined in detail in this study, along with their connection to the Aragonite Sea II to Calcite Sea II transition. According to the results, ooid abundance and size show noteworthy variations over the Oxfordian and Kimmeridgian periods, with a general rise in size during the latter. This pattern is consistent with worldwide Jurassic data and points to a connection between environmental factors, carbonate saturation, and seawater chemistry.

The Belluno Basin ooids are primarily composed of calcite, as shown by petrographic investigations. This supports the idea that the shift from aragonite to calcite sea was completed by the Oxfordian.
Overall, by emphasizing the intricate relationships between seawater chemistry, sedimentary processes, and paleoenvironmental changes, these findings advance our understanding of Jurassic carbonate sedimentation. The results support the importance of using ooids as proxies for reconstructing past oceanographic conditions and further refining the timeline of the Jurassic carbon cycle.

To build upon these findings, future research should focus on, resolving the uncertainty on biostratigraphy, especially in the first part of the log, to confirm if the log can identify partially to the Callovian age.

Post-depositional alterations influencing ooid mineralogy and preservation may be clarified by a more thorough diagenetic investigation, maybe combining cathodoluminescence (CL) and fluid inclusion investigations. CL can differentiate between various carbonate minerals based on their luminescent properties. This method helps identify primary mineral phases and detect diagenetic overprints. For instance, in a study on Cambrian micritic ooids, CL was utilized to distinguish between autochthonous micrites and those altered during diagenesis (Zhang et al., 2023).
Also using automated image analysis to measure the ooid size would allow us to measure a larger number of ooids, like in the case of the Koeshidayatullah et al. study (2022).

Finally, expanding the stratigraphic coverage would be desirable, to further investigate regional and global trends in ooid development by looking into other Belluno Basin sections and comparing them with other Tethyan sites.

References

Bathurst, R. G. C. (1975). Carbonate Sediments and Their Diagenesis. Elsevier.

Bernoulli, D., & Jenkyns, H. C. (1974). Alpine, Mediterranean, and Central Atlantic Mesozoic facies in relation to the early evolution of the Tethys. In R. H. Dott & R. H. Shaver (Eds.), Modern and Ancient Geosynclinal Sedimentation (pp. 129–160). SEPM Special Publication No. 19. https://doi.org/10.2110/pec.74.19.0129

Bernoulli, D., & Peters, T. (1970). Traces of rhyolitic-trachytic volcanism in the Upper Jurassic of the Southern Alps. Eclogae Geologicae Helvetiae, 63, 609–621.

Bertotti, G., Picotti, V., Bernoulli, D., & Castellarin, A. (1993). From rifting to drifting: Tectonic evolution of the South-Alpine upper crust from the Triassic to the Early Cretaceous. *Sedimentary Geology*, *86*(1), 53–76. https://doi.org/10.1016/0037-0738(93)90133-P

Bosellini, A., & Masetti, D. (2006). Ambiente e dinamica deposizionale del Calcare del Vajont (Giurassico medio, Prealpi Bellunesi e Friulane). Annali dell'Università di Ferrara, Sezione Scienze Geologiche e Paleontologiche, 5, 87–100.

Bosellini, A., Masetti, D., & Sarti, M. (1981). A Jurassic "Tongue of the Ocean" infilled with oolitic sands: The Belluno Trough, Venetian Alps, Italy. *Marine Geology*, *44*(1–2), 59–95. https://doi.org/10.1016/0025-3227(81)90113-4

Brigaud, B., Pucéat, E., Pellenard, P., Vincent, B., & Joachimski, M. M. (2008). Climatic fluctuations and seasonality during the Late Jurassic (Oxfordian–Early Kimmeridgian) inferred from δ18O of Paris Basin oyster shells. Earth and Planetary Science Letters, 273(1–2), 58–67. https://doi.org/10.1016/j.epsl.2008.06.020

CarbonateWorld. (n.d.). Radial ooids from the Pennsylvanian of Asturias, Northern Spain. Retrieved January 1, 2025, from https://carbonateworld.com

Casellato, C. E. (2010). Calcareous nannofossil biostratigraphy of Upper Callovian–Lower Berriasian successions from the Southern Alps, North Italy. *Rivista Italiana di Paleontologia e Stratigrafia, 116*(3), Article 3. https://doi.org/10.13130/2039-4942/6394

Castellarin, A., Cantelli, L., Fesce, A. M., Mercier, J. L., Picotti, V., Pini, G. A., Prosser, G., & Selli, L. (1992). Alpine compressional tectonics in the Southern Alps: Relationships with the N-Apennines. Annales Tectonicae, 6(1), 62–94.

Chiari, M., Cobianchi, M., & Picotti, V. (2007). Integrated stratigraphy (radiolarians and calcareous nannofossils) of the Middle to Upper Jurassic Alpine radiolarites (Lombardian Basin, Italy): Constraints to their genetic interpretation. *Palaeogeography, Palaeoclimatology,Palaeoecology*,*249*(3),233–270. https://doi.org/10.1016/j.palaeo.2007.02.001

Cobianchi, M. (2002). I nannofossili calcarei del Giurassico medio e superiore del bacino di Belluno (Alpi Calcaree Meridionali). Atti Ticinensi di Scienze della Terra, 43, 3–24.

Cobianchi, M., & Picotti, V. (2002). The Vajont Gorge section: The Toarcian to Bajocian Igne Formation and the unconformable base of the Vajont Limestone. In M. Santantonio (Ed.), 6th International Symposium on the Jurassic System, General Field Trip Guidebook (pp. 310–317). Palermo, Italy.

Coplen, T.B., Brand, W.A., Gehre, M., Groning, M., Meijer, H.A.J., Toman, B., & Verkouteren, R.M., (2006). New guidelines for d13C measurements. Anal. Chem. 78, 2439e2441. http://dx.doi.org/10.1021/ac052027c.

Della Bruna, G., & Martire, L. (1985). La successione giurassica (Pliensbachiano–Kimmeridgiano) delle Alpi Feltrine (Belluno). Rivista Italiana di Paleontologia e Stratigrafia, 91(1), 15–62.

Dera, G., Brigaud, B., Monna, F., Laffont, R., Puceat, E., Deconinck, J.-F., Pellenard, P., Joachimski, M. M., & Durlet, C. (2011). Climatic ups and downs in a disturbed Jurassic world. *Geology*, *39*(3), 215–218. https://doi.org/10.1130/G31579.1

Fischer, A. G. (1982). Long-term climatic oscillations recorded in stratigraphy. *In Climate in Earth History: Studies in Geophysics* (pp. 97-104). National Academy Press.

Flügel, E. (2010). *Microfacies of Carbonate Rocks: Analysis, Interpretation and Application*. Springer. https://doi.org/10.1007/978-3-642-03796-2 https://books.google.it/books/about/Microfacies_of_Carbonate_Rocks.html?id=Rbq4KJETsVwC&redir_esc=y

Google Earth. (2025). [Satellite imagery of Trovena Hamlet, Italy]. Retrieved January 4, 2025, from https://earth.google.com/

Howes, B., Mehra, A., & Maloof, A. C. (2021). Three-dimensional morphometry of ooids in oolites: A new tool for more accurate and precise paleoenvironmental interpretation. Journal of Geophysical Research: Earth Surface, 126, e2020JF005601. https://doi.org/10.1029/2020JF005601

Husinec, A., Read, J. F., & Prtoljan, B. (2022). Middle and Late Jurassic record of sea-level, sequence development, and carbon-isotope fluctuations, Tethyan Adriatic Carbonate Platform, Croatia. Palaeogeography, Palaeoclimatology, Palaeoecology, 599, 111033. https://doi.org/10.1016/j.palaeo.2022.111033

James, N. P., Bone, Y., & Kyser, T. K. (1999). Echinoderm contributions to a cool-water carbonate factory: Low-Mg calcite secrets. Geology, 27(8), 635–638. https://doi.org/10.1130/0091-7613(1999)027<0635:ECTACW>2.3.CO;2

Jenkyns, H. C., Jones, C. E., Gröcke, D. R., Hesselbo, S. P., & Parkinson, D. N. (2002). Chemostratigraphy of the Jurassic System: Applications, limitations and implications for palaeoceanography. Journal of the Geological Society, 159(4), 351–378. https://doi.org/10.1144/0016-764901-130

Kiessling, W. (2009). Geographical distribution and time dependence of global carbonate platform accumulation. Sedimentary Geology, 219(1-4), 15–28. https://doi.org/10.1016/j.sedgeo.2009.04.017

Kim, S.-T., Coplen, T.B., & Horita, J. (2015). Normalization of stable isotope data for carbonate minerals: implementation of IUPAC guidelines. Geochim. Cosmo chim. Acta 158, 276e289. http://dx.doi.org/10.1016/j.gca.2015.02.011.

Koeshidayatullah, A., Trower, E. J., Li, X., Mukerji, T., Lehrmann, D. J., Morsilli, M., Al-Ramadan, K., & Payne, J. L. (2022). Quantitative evaluation of the roles of ocean chemistry and climate on ooid size across the Phanerozoic: Global versus local controls. Sedimentology, 69(6), 2486–2506. https://doi.org/10.1111/sed.12998

Masetti, D., Claps, M., Giacometti, A., Lodi, P., & Pignatti, P. (1998). I Calcari Grigi della Piattaforma di Trento (Lias Inferiore e Medio, Prealpi Venete). Atti Ticinensi di Scienze della Terra, 40, 139–183.

Masetti, D., Fantoni, R., Romano, R., Sartorio, D., & Trevisani, E. (2012). Tectonostratigraphic evolution of the Jurassic extensional basins of the eastern southern Alps and Adriatic foreland based on an integrated study of surface and subsurface data. *AAPG Bulletin*, *96*(11), 2065–2089. https://doi.org/10.1306/03091211087

Mattioli, E., & Erba, E. (1999). Synthesis of calcareous nannofossil events in Tethyan Lower and Middle Jurassic successions. Rivista Italiana di Paleontologia e Stratigrafia, 105, 345–376.

Muttoni G., Erba E., Kent D., Bachtadse V. (2005). Mesozoic Alpine Facies Deposition As a Result of Past Latitudinal Plate Motion. Nature, Vol. 434, No. 7029, 2005, pp. 59-63. http://dx.doi.org/10.1038/nature03378.

Nicosia, U., & Parisi, G. (1979). Saccocoma tenella (Goldfuss)—Distribuzione stratigrafica e geografica. Bollettino della Società Paleontologica Italiana, 18, 320–326.

Picard, S., Garcia, J. P., Lécuyer, C., Sheppard, S. M. F., Cappetta, H., & Emig, C. C. (1998). $\delta^{18}O$ values of coexisting brachiopods and fish: Temperature differences and estimates of paleo-water depths. Geology, 26(11), 975–978. https://doi.org/10.1130/0091-7613(1998)026<0975:OVOCBA>2.3.CO;2

Picotti, V., & Cobianchi, M. (2017). Jurassic stratigraphy of the Belluno Basin and Friuli Platform: A perspective on far-field compression in the Adria passive margin. Swiss Journal of Geosciences, 110(3), 833–850. https://doi.org/10.1007/s00015-017-0268-3

Rankey, E. C., & Reeder, R. J. (2000). Radial and tangential ooids: Mineralogy and microstructure. Journal of Sedimentary Research, 70(3), 538–548. https://doi.org/10.1306/2DC4092E-0E47-11D7-8643000102C1865D

Sandberg, P. (1983). An oscillating trend in Phanerozoic nonskeletal carbonate mineralogy. Nature, 305, 19–22. https://doi.org/10.1038/305019a0

Stefani, C., Fellin, M. G., Zattin, M., Zuffa, G. G., Dalmonte, C., Mancin, N., & Zanferrari, A. (2007). Provenance and paleogeographic evolution in a multi-source

foreland: The Cenozoic Venetian-Friulian Basin (NE Italy). Journal of Sedimentary Research, 77(11), 867–887. https://doi.org/10.2110/jsr.2007.083

Trower, E. J., Smith, B. P., Koeshidayatullah, A., & Payne, J. L. (2022). Marine ooid sizes record Phanerozoic seawater carbonate chemistry. Geophysical Research Letters, 49(22), e2022GL100800. https://doi.org/10.1029/2022GL100800

Tucker, M. E., & Wright, V. P. (1990). Carbonate Sedimentology. Blackwell Science.

Vulpius, D., & Kiessling, W. (2006). Jurassic ooids and the aragonite-calcite sea transition. Journal of Sedimentary Research, 76(3), 205–212. https://doi.org/10.2110/jsr.2006.018

Wilson, M. A. (n.d.). *Aragonite threshold diagram [Image].* Wikipedia. Retrieved from https://en.wikipedia.org/wiki/Calcite_sea

Winterer, E. L., & Bosellini, A. (1981). Subsidence and sedimentation on Jurassic passive continental margin, Southern Alps, Italy. AAPG Bulletin, 65(3), 394–421.

Zhang, S., Shen, Y., & Zhang, Y. (2023). Microbial origin of micrites in ooids: Evidence from the Cambrian in North China. Sedimentary Geology, 430, 106079. https://doi.org/10.1016/j.sedgeo.2023.106079

Acknowledgments

Academic..

Thanks from the bottom of my heart to my supervisor Prof. Nereo
Dr Ingrid Urban - My friend and my co-worker Mahla Moradi
Melissa Kozhaya who helped me a lot with the whole thesis and the master
Prof. Miriam Cobianchi
Leonardo Tauro, Jacopo Nava, Silvia Catto', Dr. Gaia Sartori, prof Cristina Stefani,
Thanks to my universities and all my professors through all these years here in Italy and in Egypt especially Prof. Youssef.

My beloved ones..

In Egypt: My family and my friends (papa, mama, my Aya, and her husband, my small one Anas) my sisters Fatma, Nour, and Mohammed, my grandma, Sabah, Sahar, Eabir, Doaa, Ahmed, Mahmoud, Mahmoud, Mimi, Noura, Rahma, Radwa, and their beautiful children, Youssef, Marwa, "Jowairiya", Manal, Mando, Ahmed, Karim, and their children, Alaa Salah, Miriam, Omneya, Hadir, Aya, and my co-workers.

(grandma, grandpa, Aunt Shadia)

And here: Matthew, Ima, Pa, Melissa Kozhaya and her family, Francesco, Therese, and Josef.

My friends: Nazila, Eli, Mahesh, Gihad, Ashmi, Lava, Tamana, Saye, Saradha, Andrea, Haidi, Waqar, Mohammed, Anmol, John, Bernadette, John, Magda, Yusif, Karol, Clare, Rifqa, Augustine, pio, Andrew Kim, Antonios, Anthony, Carlo, Nectarios, Karas, Nazir, Micheal, Gabrial, Gemma Also Naomi, Adila, Bernarda, Elisabetta, Maria, Anna, Nadia, Regina, Federico, Carla, Alberto, Ahmed, Nadia, Claudio ^^

Above all of the above, thank you, God... thank you a lot ♡